Journal Pre-proof

Pt nanocluster-catalyzed hydrogen evolution reaction: Recent advances and future outlook

Hongliang Zeng , Yuan Ji , Jinfeng Wen , Xu Li , Tingting Zheng , Qiu Jiang , Chuan Xia

Please cite this article as: Hongliang Zeng ,   Yuan Ji ,   Jinfeng Wen ,   Xu Li ,   Tingting Zheng , Qiu Jiang ,   Chuan Xia , Pt nanocluster-catalyzed hydrogen evolution reaction: Recent advances and future outlook, *Chinese Chemical Letters* (2024), doi: https://doi.org/10.1016/j.cclet.2024.109686

This is a PDF file of an article that has undergone enhancements after acceptance, such as the addition of a cover page and metadata, and formatting for readability, but it is not yet the definitive version of record. This version will undergo additional copyediting, typesetting and review before it is published in its final form, but we are providing this version to give early visibility of the article. Please note that, during the production process, errors may be discovered which could affect the content, and all legal disclaimers that apply to the journal pertain.
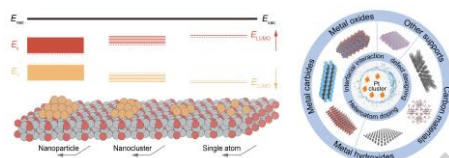
Graphical Abstract

Pt nanocluster-catalyzed hydrogen evolution reaction: Recent advances and future outlook

Hongliang Zeng[a], Yuan Ji[a], Jinfeng Wen[a], Xu Li[a], Tingting Zheng[a], Qiu Jiang[a,b,*], Chuan Xia[a,b,*]

[a] *School of Materials and Energy, University of Electronic Science and Technology of China, Chengdu 611731, China*
[b] *Yangtze Delta Region Institute (Huzhou), University of Electronic Science and Technology of China, Huzhou 313001, China*

We offer a comprehensive summary encompassing the strategies utilized in synthesis, the conducted structural analyses, and the observed performance metrics for Pt nanocluster catalysts in conjunction with diverse supporting materials.

2

Chinese Chemical Letters

Pt nanocluster-catalyzed hydrogen evolution reaction: Recent advances and future outlook

Hongliang Zeng[a], Yuan Ji[a], Jinfeng Wen[a], Xu Li[a], Tingting Zheng[a], Qiu Jiang[a,b,∗], Chuan Xia[a,b,∗]

[a] School of Materials and Energy, University of Electronic Science and Technology of China, Chengdu 611731, China
[b] Yangtze Delta Region Institute (Huzhou), University of Electronic Science and Technology of China, Huzhou 313001, China

ARTICLE INFO

ABSTRACT

As hydrogen energy technologies gain momentum, the role of renewable energy in facilitating sustainable hydrogen production is becoming increasingly critical. As a hydrogen production method, water electrolysis has attracted much attention from researchers due to its operational simplicity, the high purity of the hydrogen generated, and its potential for achieving zero carbon emissions throughout the process. Numerous studies has been manipulated on platinum (Pt)-based catalysts, which exhibit superior performance in hydrogen evolution reactions. Within this category, Pt nanoclusters stand out due to their unique attributes, such as quantum size effects and unique coordination environments. These features enable them to outperform both Pt metal atoms and nanoparticles in hydrogen evolution reactions regarding activity and stability. Here, we primarily delve into the reaction mechanisms underlying Pt nanocluster-based hydrogen catalysts, with particular emphasis on the interactions between the metal catalysts and their associated support materials. We provide an exhaustive summary of the strategies employed in the synthesis, the structural analyses conducted, and the performance metrics observed for Pt nanocluster catalysts when paired with various supporting materials. In closing, we explore the future potential and challenges facing Pt nanocluster-based catalysts in the context of industrial water electrolysis, along with emerging avenues for their design and optimization.

1. Introduction

The relentless rise in energy demand has accelerated the consumption of conventional fossil fuels, thereby exacerbating global environmental deterioration [1–5]. As a result, the pursuit of sustainable, eco-friendly energy sources and efficient energy storage and conversion technologies are now imperative for fostering sustainable development [6–12]. Hydrogen has numerous advantages over other renewable energy sources (*e.g.*, solar, wind, tidal). It not only has a high energy density, but also produces only water as a byproduct, minimizing its environmental impact [13–17]. Presently, approximately 90% of hydrogen production is generated through the process of reforming fossil fuels, which includes sources such as coal, oil, natural gas, and byproducts from various industries. While this method is prevalent, it poses significant environmental challenges. The preparation process not only results in substantial pollution but also generates large volumes of CO_2 gas, exacerbating global greenhouse gas emissions [18]. In contrast, the generation of "green hydrogen" through the use of renewable energy sources represents a more sustainable and environmentally responsible approach [19–26]. Among these methods, electrolyzing water to produce hydrogen stands out for its diverse array of advantages, such as high hydrogen purity, high scalability, and ease of integration with renewable energy systems for grid balancing and energy storage [12,27,28]. Despite these benefits, the scalability of water electrolysis remains constrained by the performance of the electrocatalysts employed in electrode reactions [29]. At present, platinum (Pt) remains the best cathode catalyst for the hydrogen evolution reaction (HER) because of its optimal hydrogen adsorption Gibbs free energy (ΔG_{H*}) [30,31]. Nevertheless, the considerable expense of Pt poses a notable challenge, with commercial Pt/C cathode catalysts requiring as much as 0.4-0.6 mg/cm^2 of the material [32].

Various approaches have been explored to minimize Pt loading, primarily focusing on enhancing the intrinsic catalytic performance and optimizing the utilization of active sites. These strategies include rationally designing the catalyst morphology and downsizing the catalyst to nanometer dimensions [30,33–35]. In the case of bulk metals, such as Pt slab, the band structure is continuous, with free electrons exhibiting oscillatory behavior. However, upon size reduction to the nanocluster scale, there is a splitting of energy at the Fermi level and further changed to Free-atom-like d states for single atoms. This change significantly affects the density of valence states. As a result, the transition from a continuous density of states in bulk metals to discrete energy levels in nanoclusters leads to more pronounced quantum properties and distinct catalytic performance [36]. Generally, large Pt nanoparticles are less effective at achieving high HER activity, primarily because of their finite specific surface area, resulting in a scarcity of exposed active sites [35,37].

∗ Corresponding authors.
E-mail addresses: chuan.xia@uestc.edu.cn (C. Xia), jiangqiu@uestc.edu.cn (Q. Jiang).

Reducing the particle size enhances both the utilization and dispersion of active sites; however, this comes at the expense of stability. For instance, while Pt single atoms can essentially expose all their active sites, they are prone to agglomeration because of their high surface free energy. This agglomeration subsequently results in a decrease in catalytic activity [38]. Compared to nanoparticles and single atoms, Pt nanoclusters offer a more balanced profile of attributes. The unique electronic properties of these materials, coupled with their quantum size and surface geometric effects, contribute to stronger electronic interactions with supporting materials. This facilitates optimal charge transfer, thereby enhancing the structural stability of the nanoclusters. Therefore, Pt nanoclusters can achieve both structural stability and HER catalytic activity. These characteristics position Pt nanoclusters as a promising avenue for real applications in sustainable hydrogen production (Fig. 1) [39–43].
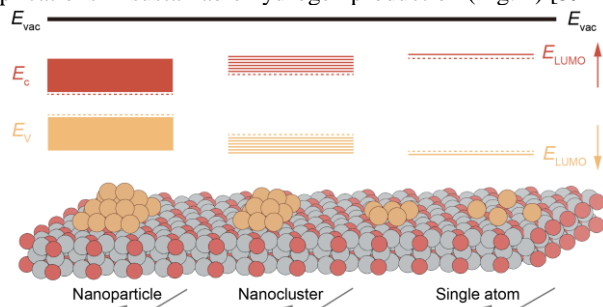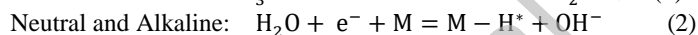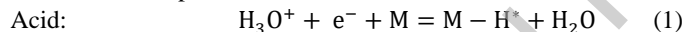

Fig. 1. Schematic representation of the relationship between the electronic structure and size in Pt catalysts.

In this review, we will begin by providing an overview of the HER mechanism and then delve into a discussion of the distinctive properties of Pt nanoclusters that enable and enhance their role in HER facilitation. We will then systematically summarize the synthesis approaches, structural analyses, and electrocatalytic performance of Pt nanoclusters when they are employed with various support materials, including transition metal compounds, carbon materials, and other amorphous substrates. In conclusion, we will delve into the future prospects and challenges of Pt nanocluster-based catalysts within the realm of industrial water electrolysis. Furthermore, we intend to offer insights into possible avenues for future research and development in this area.
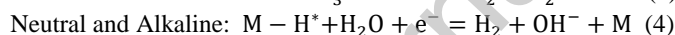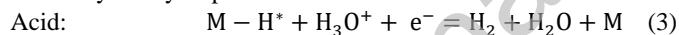
2. The HER mechanism

Electrochemical water reduction is a pivotal half-reaction in the process of hydrogen generation at the cathode [29]. In different electrolytes (H_3O^+ as a reactant in acidic media, H_2O as a reactant in neutral and alkaline media), the generally accepted HER mechanism on the catalyst surface involves three basic steps: the Volmer step, the Heyrovsky step and the Tafel step [44].

- Volmer step

Acid: $\qquad H_3O^+ + e^- + M = M - H^* + H_2O \qquad$ (1)

Neutral and Alkaline: $\quad H_2O + e^- + M = M - H^* + OH^- \qquad$ (2)

- Heyrovsky step

Acid: $\qquad M - H^* + H_3O^+ + e^- = H_2 + H_2O + M \quad$ (3)

Neutral and Alkaline: $\ M - H^* + H_2O + e^- = H_2 + OH^- + M$ (4)

- Tafel step

Acidic, Neutral and Alkaline: $\quad 2M - H^* = H_2 + 2M \qquad$ (5)

In the HER process under all conditions, the hydrogen intermediate (H*) attached to the catalyst surface originates from the merging of a hydrated hydrogen ion with an electron. Subsequently, H_2 is produced through either the Heyrovsky step or the Tafel step (Fig. 2) [31]. Notably, regardless of the specific reaction pathway within the HER process, the involvement of H* is a common feature. Additionally, the Volmer, Heyrovsky, or Tafel reactions could each act as kinetic rate-limiting steps in the HER. The Tafel equation is instrumental in determining which step is rate-limiting. Commonly, Tafel slopes of approximately 120, 40, or 30 mV/dec suggest that the rate-limiting steps correspond to the Volmer, Heyrovsky, or Tafel reactions, respectively [45].
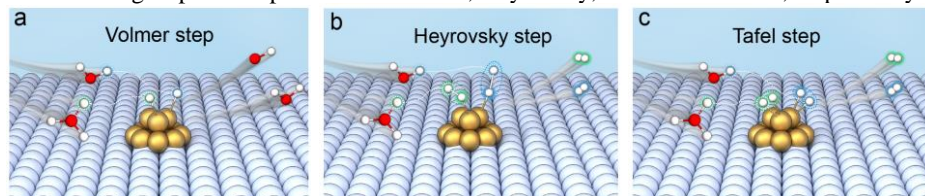

Fig. 2. The kinetic mechanisms of the HER, including (a) the Volmer, (b) Heyrovsky, and (c) Tafel processes.

According to the Sabatier principle, the hydrogen binding energy (HBE) plays a vital role in the catalytic activity of the HER [46]. When the HBE is too low on the catalyst surface, the adsorption of H* becomes inefficient. On the other hand, an excessively strong HBE hinders the release of H* from the catalyst surface [47]. Therefore, the optimal HBE (where ΔG_{H*} is close to zero) is essential, as it strikes a balance between these two fundamental steps, as outlined by the Sabatier principle [47,48]. The volcano plot in Fig. 3, which combines HBE and ΔG_{H*} from experimental and theoretical calculations, allows for the evaluation of catalyst activity. It is evident that the Pt group noble metals (PGMs), with Pt as a representative, exhibit the highest activity and are among the most promising HER catalysts [49,50]. Specifically, compared with other noble-metal-based catalysts (Table 1) [35,41,51–56], Pt-based catalysts demonstrate notable superiority across several parameters, such as reaction kinetics, HER activity, and stability.
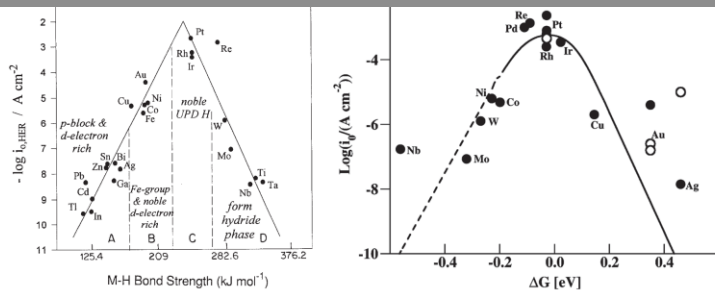
Fig. 3. A volcano plot depicting $\log(i_0)$ values as related to (a) the energy of the metal–hydrogen bond and (b) ΔG_{H*}. Copied with permissions [49,50], Copyright 2000, Elsevier. Copyright 2000, American Chemical Society.

Table 1
Comparison of the performance among different noble-metal-based catalysts (tested in three-electrode systems).

Catlayst	Noble metal loading ($\mu g/cm^2$)	Tafel slope (mV/dec)	Overpotential (mV) @10 mA/cm^2	Stability (h)	Ref.
	/	12	18	20	[35]
Pt nanocluster-based catalysts	2.55	23.51	11	/	[41]
	/	78	62	800	[51]
	44	40.99	6.9	24	[52]
	/	21	19	22	[53]
Other-noble-metal-based catalysts (Rh/Ir/Ru)	213.03	27.5	23.3	200	[54]
	73.3	21.2	22	17	[55]
	10	35.2	50.4	6	[56]

3. Unique electronic and geometric configurations of Pt nanoclusters

When the dimensions of a metallic material are diminished to a specific critical range, a marked alteration in its chemical properties is invariably observed. Correspondingly, nanocatalysts exhibit distinct physicochemical characteristics that significantly differ from those of their bulk material counterparts [57]. This pivotal discovery has catalyzed renewed interest in the structural and electronic states of nanocatalysts. Theoretically, when the dimensions of metallic nanoparticles are reduced to a scale smaller than the de Broglie wavelength of electrons, disintegration of the conventional band structure ensues, leading to quantum confinement phenomena. In this regime, sub-nanometer clusters may exhibit a plethora of isomeric configurations analogous to molecular isomers. These isomeric states are characterized by disparate molecular orbitals, the geometries of which are contingent upon their respective electronic states. This intricate interplay between electronic and structural properties at the sub-nanometer scale elucidates new dimensions in the scientific understanding and potential technological utilization of nanoscale metallic catalysts. As a result, the electronic structure of nanoclusters transitions between molecular split energy levels and solid continuous energy bands (Fig. 1) [58].

Unlike mononuclear metal complexes, where the electronic structure is intrinsically tied to the coordination environment influenced by ligands and solvents [59], metal clusters exhibit markedly different behaviors. Specifically, the work function in these clusters significantly varies based on the number of constituent atoms. This variability arises from the orbital overlap between metal atoms within the cluster. Such orbital interactions engender unique electronic properties, thereby differentiating metal clusters from their mononuclear counterparts in terms of both their electronic structure and associated reactivity [60]. By judiciously modulating both the atomic composition and geometric configuration of metal clusters, it is possible to engineer a highly unsaturated coordination environment. This specialized coordination milieu fosters robust interactions with different molecules, thereby potentially enhancing the catalytic efficacy and selectivity of the cluster [61]. For instance, a metal cluster of a specific atomicity, such as Au_7, can manifest in multiple geometric configurations (the geometries of Au_{7-}, Au_7, and Au_{7+} differ owing to variations in their charge states) [62,63]. Such flexibility in charge states affords a dynamic means of modulating the catalytic property of clusters within electrochemical processes [64]. Zhang *et al.* [65] provided empirical and theoretical evidence underscoring the size-dependent activity and stability of Pt nanoclusters over Pt single atoms (Pt_1) and bulk Pt. Experimentally, they evaluated the electrochemical performance of variously sized platinum (Pt) nanoparticles, specifically Pt_1, Pt_4, Pt_7, and Pt_8, by methodically controlling the Pt loading on fluorine-doped tin oxide (FTO) substrates. The results indicated a clear trend in mass activity: $Pt_1 < Pt_4 \approx Pt_{poly} < Pt_7 \approx Pt_8$. Furthermore, hydrogen underpotential deposition (H_{UPD}) analysis revealed that, when compared to those of Pt_1 and polycrystalline Pt, Pt clusters (Pt_7 and Pt_8) demonstrated the highest H_{UPD} currents. Theoretically, using DFT calculations, they analyzed the size-dependent HER activity under varying conditions. At high H coverage, compared with larger clusters (Pt_7 and Pt_8), Pt_1 is more susceptible to the weakening of Pt-O bonds since there are no Pt-Pt bonds to stabilize it; thus, Pt_1 is expected to be more easily soluble and less stable. On the other hand, the strengths of Pt-Pt and Pt-O bonds were found to not exhibit a monotonic relationship with the size of the clusters. Specifically, the strength of Pt-Pt bonds follows the order $Pt_4 > Pt_8 \approx Pt_7$. This aligns with the trend in HER activity and stability trend $Pt_4 < Pt_7 < Pt_8$. The reasons behind these trends are intricate and were attributed to the concept of "ensemble size". Yan *et al.* [41] also experimentally discovered that electron-rich Pt nanoclusters have better HER performance than oxidized Pt single atoms and particles. Specifically, in the case of Pt single atoms, there is a transfer of electrons from the Pt to the sulfur-doped carbon supports. Conversely, when the size of the Pt reduces to clusters, the carbon supports donate electrons to the Pt. As a result, electron-enriched Pt nanoclusters demonstrate significantly higher HER activity compared to electron-deficient Pt single atoms.

To conclude, the geometric structure of metal nanoparticles is more stable than that of single atoms. This enhanced stability primarily arises from the reduced surface energy associated with the higher coordination environment. However, metal nanoparticles with high coordination numbers have lower lying d-bands, which leads to lower activity [66]. In contrast, Pt nanoclusters strike a balance,

possessing suitable surface-free energy and relatively lower surface coordination. This unique combination allows them to maintain a relatively more stable structure while also preserving robust electrocatalytic activity. Consequently, for Pt nanoclusters as HER catalysts, a detailed examination of the activity modulations attributable to their inherent electronic and geometric peculiarities is imperative. This investigation is essential for a comprehensive understanding of the catalytic efficiency mechanisms inherent in Pt nanoclusters and is instrumental in advancing the development of next-generation, high-performance catalysts for hydrogen evolution.

4. Identification of metal-support interactions

Pt nanoclusters are an important type of hydrogen evolution catalyst due to their unique size, shape, and composition controllability. Several strategies have been developed to engineer and modulate these properties. One of the key strategies is to immobilize Pt nanoclusters on supports to enhance their stability and control their spatial distribution. However, it is important to note that the support material is typically not inert, and the interplay between Pt and its supporting material can give rise to new interfacial phenomena, collectively referred to as metal-support interactions (MSIs) [42]. MSIs have an important impact on the electronic properties of catalysts. Typical MSI phenomena involve elements such as charge transfer [39,43,67,68], interfacial sites [35,41,69–72], and strong metal-support interaction (SMSI) (Fig. 4a) [73–76]. These elements often interact together to promote the catalytic performance of electrochemical hydrogen evolution.

Yan *et al.* [41] demonstrated that HER catalysts with Pt clusters confined on sulfur-doped carbon supports had a joint effect on charge transfer and interfacial sites through experimental characterization and theoretical calculations. Clearly, in comparison to the Pt cluster directly supported on carbon black (PtNC/BP2000), the PtNC/S-C catalyst exhibited a lower binding energy, as indicated by the X-ray photoelectron spectroscopy (XPS) results (Fig. 4b). Additionally, the normalized X-ray absorption near edge structure (XANES) spectra of PtNC/S-C demonstrated a reduced white line intensity relative to that of PtNC/BP2000 (Fig. 4c), suggesting that the S sites are favorable for providing electrons to Pt nanoclusters due to carrier transfer. In addition, Bard charge analysis also demonstrated that single-atom Pt and Pt clusters have diametrically opposite charge transfer directions from the support, thereby achieving different electrocatalytic hydrogen evolution properties (Fig. 4d).

Additionally, when Pt clusters engage with the support material, electronic reconfiguration occurs. This leads to either an upward or downward shift in the d-band center of platinum, affecting the adsorption characteristics of the reaction intermediates, which in turn impacts the electrocatalytic performance. According to the d-band theory, the strength of intermediate adsorption is directly correlated with the position of the antibonding band. (Fig. 4e) [77]. An increased electron occupancy in the antibonding energy band diminishes the portion of the band situated above the Fermi energy level. This leads to less stable bonding interactions and consequently results in weaker adsorption of reaction intermediates. Wu *et al.* [35] illustrated the interaction between Pt clusters and different supports by partial density of states (PDOS) analysis. This analysis showed that Pt/TiO_2-O_v exhibited a lower d-band center than Pt/TiO_2, implying a reduced strength in hydrogen adsorption (Fig. 4f). A further comparison of the hydrogen adsorption free energies revealed that Pt/TiO_2-O_v had the weakest adsorption of hydrogen, which is consistent with the d-band theory (Fig. 4g). These results illustrated the influence of interfacial oxygen vacancies on the metal-support interaction, promoting the hydrogen evolution performance of the catalyst.
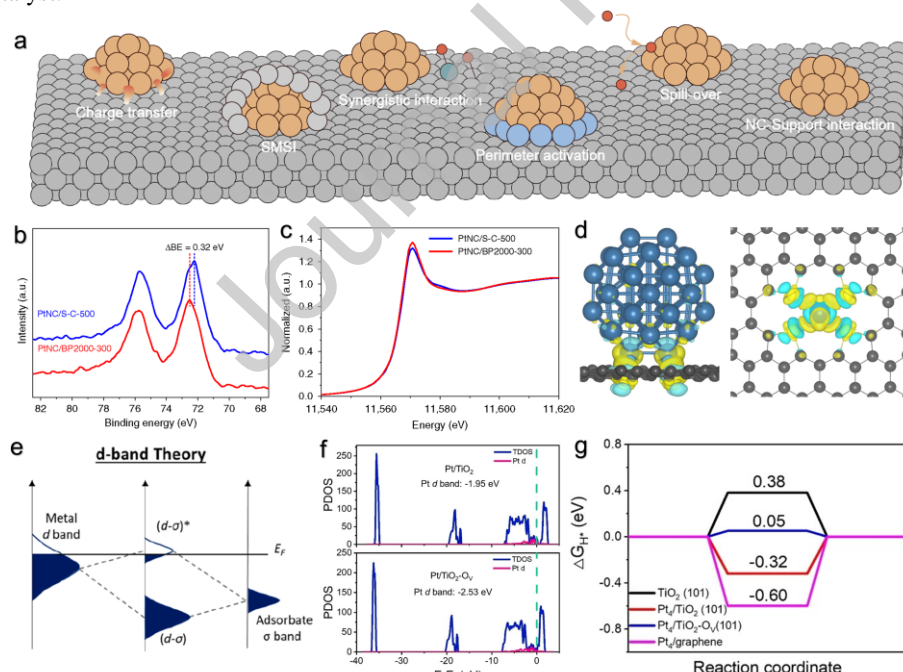

Fig. 4. (a) Schematic showing the typical metal-support interaction types. (b) High-resolution XPS spectra (Pt 4f) and (c) normalized XANES spectra (Pt L_3-edge) for PtNC/BP2000-300 and PtNC/S–C-500. (d) Analysis of differential charge density in the PtNC/S-C and Pt_1/S-C systems. In this analysis, positive and negative electron density isosurfaces are represented by yellow and cyan colors, respectively. (b-d) Copied with permission [41]. Copyright 2019, Nature Portfolio. (e) A diagrammatic representation of the d-band theory model, Copied with permission [77]. Copyright 2022, American Chemical Society. (f) The PDOS (Pt 5d) comparison between Pt/TiO_2 and Pt/TiO_2-O_v. (g) The calculated ΔG_{H*} values for TiO_2, Pt/TiO_2, Pt/TiO_2-O_v and Pt/graphene. Copied with permission [35]. Copyright 2023, Wiley-VCH.

Pt nanoclusters possess distinct morphological and structural attributes, enabling them to pair effectively with a diverse range of support materials to achieve commendable electrocatalytic performance in hydrogen evolution. Specifically, fine-tuning the nature of the interactions between Pt nanoclusters and different supports—including metal oxides, carbides, hydroxides, and carbon-based materials—can further enhance the efficacy of catalysts in the HER (Fig. 5). Subsequently, a clear elucidation of the catalytic reaction mechanism becomes possible, offering valuable insights that can guide the design of next-generation Pt nanocluster-based catalysts for hydrogen evolution.
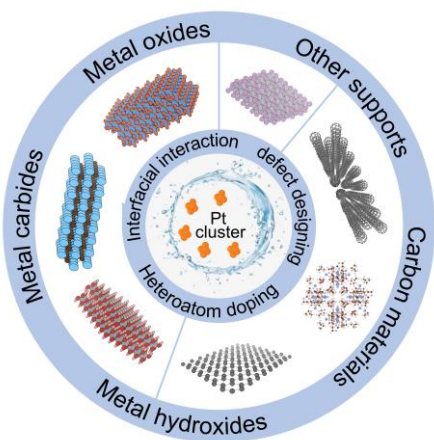

Fig. 5. Diagram of the supports for anchoring Pt nanoclusters, including metal oxides, carbides, hydroxides, and carbon materials.

5.1 Pt nanocluster-based oxide electrocatalyst

5.1.1 Interfacial interaction

Metal oxides have become one of the important supports for hydrogen evolution catalysts due to their chemical inertness, porosity and high electrical conductivity [78]. For decades, a variety of metal (Ti, Sn, Mn, Nb, and W) oxides have been used as supports in electrocatalytic reactions [74,79–82]. The activity of the composite catalysts is enhanced through interfacial interactions after hybridization with Pt nanoclusters [83,84].

Cheng *et al*. [83] obtained a PtO_x/TiO_2 catalyst by an impregnation method, and the Pt nanoclusters (~0.75 nm) were isolated and scattered on the surface of TiO_2 (Fig. 6a). XANES spectroscopy revealed that PtO_x/TiO_2 exhibited a white line intensity close to that of PtO_2, indicating that the Pt nanoclusters in PtO_x/TiO_2 were in an oxidized state (Fig. 6b). Interestingly, the size of the Pt nanoclusters in PtO_x/TiO_2 basically did not change before and after accelerated degradation tests (ADT) (Fig. 6c); the primary cause is likely SMSI between the oxidized Pt nanoclusters and TiO_2, which restricts the movement and clustering of the Pt clusters. In addition, Kim *et al*. [84] prepared $F-SnO_2$ with high conductivity by the sol-gel method, and further obtained uniformly dispersed Pt nanoclusters by ion sputtering (Fig. 6d). Interestingly, in the XPS spectrum, they found that Pt on Pt/SnO_2 has a lower 4f orbital binding energy than Pt foil, and with the decrease in F, the binding energy of Pt further decreases (Fig. 6e). A comparison of the PDOS and ΔG_{H^*} data showed that $Pt/F-SnO_2$ has the weakest adsorption of hydrogen intermediates (H*), which is more conducive to the HER (Fig. 6f). These findings suggest that interfacial SMSI is vital for improving the HER performance of composite catalysts.
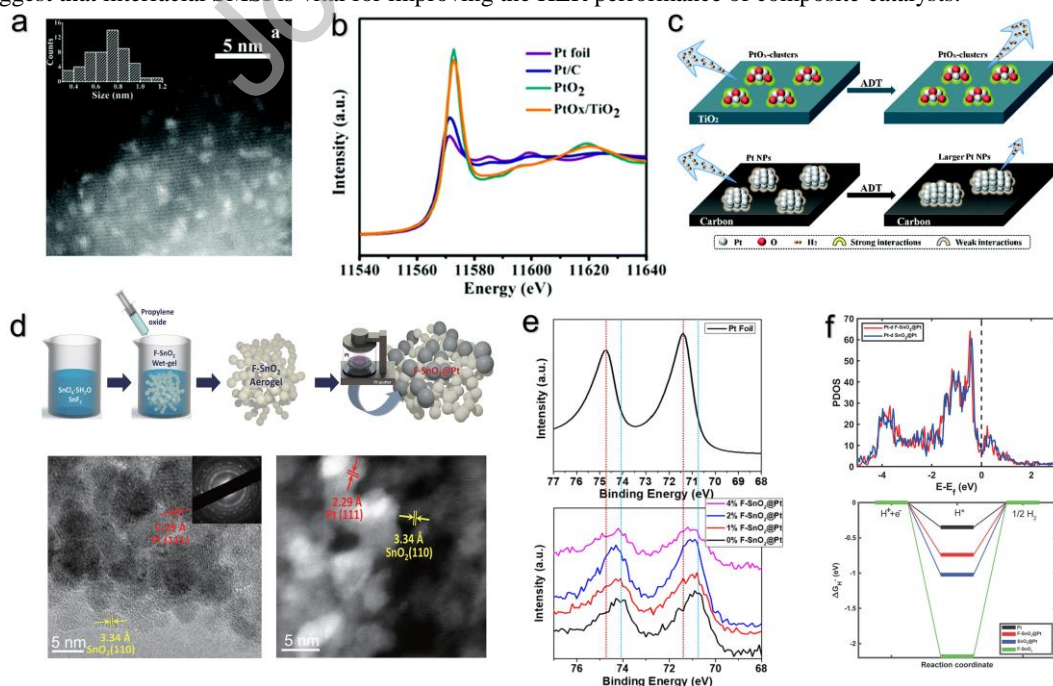

Fig. 6. (a) Scanning transmission electron microscopy (STEM) images of PtO_x clusters on PtO_x/TiO_2. (b) Normalized XANES spectra (Pt L_3-edge) for various Pt forms. (c) structural changes of PtO_x/TiO_2 and Pt/C after ADT. (a-c) Copied with permission [83]. Copyright 2017, Royal Society of Chemistry. (d) A

schematic diagram of the synthesis of highly dispersed Pt nanoclusters loaded on F-doped SnO$_2$ aerogel (upper part), below shows the HRTEM and HAADF-STEM images. (e) High-resolution XPS spectra (Pt 4f) of F-doped F-SnO$_2$@Pt with different F concentrations, Pt foil is shown as a reference. (f) PDOS analysis (d-orbital of Pt) in F-SnO$_2$@Pt and SnO$_2$@Pt (upper part), Comparison of ΔG_{H*} of different system (Pt slab, SnO$_2$@Pt, F-SnO$_2$@Pt, and F-SnO$_2$) (lower part). (d-f) Copied with permission [84]. Copyright 2022, American Chemical Society.

5.1.2 Defect design

Defects present in the support material are crucial for optimizing both the structural stability and the catalytic efficiency of the catalyst. [51]. These defective sites can not only fill the deposited metal nanoclusters but also change the coordination environment of the catalyst, which is beneficial for activating the adsorbed reactants [35,82,85,86]. Wu *et al*. [35] designed a black TiO$_2$-supported Pt cluster with abundant oxygen vacancies (Pt/TiO$_2$-O$_v$) (Fig. 7a). The TEM image showed that the size of the Pt nanoclusters of Pt/TiO$_2$-O$_v$ was between 1 ~ 2 nm. Further electron paramagnetic resonance (EPR) illustrated that the g value of Pt/TiO$_2$-O$_V$ is 2.002, which is mainly due to the binding between superoxide radicals ($O_2^{\cdot-}$) and oxygen vacancies (O$_{Vs}$) on the outer surface of the metal oxide (Fig. 7b) [87,88]. They found that the adsorption energy of Pt nanoclusters on Pt/TiO$_2$-O$_v$ was the most negative (−6.87 eV), confirming the strong metal-support interaction (Fig. 7c). Wei *et al*. [85] further developed catalysts characterized by oxygen-rich vacancies and oxygen-deficient vacancies, specifically V$_O$-rich Pt/TiO$_2$ and V$_O$-deficient Pt/TiO$_2$ (Figs. 7d and e). The average size of the Pt particles was only 0.8 nm (Fig. 7e). Compared with V$_O$-deficient Pt/TiO$_2$ and Pt/C, V$_O$-rich Pt/TiO$_2$ exhibited the best hydrogen evolution activity (Fig. 7f). These results indicate that regulating the oxygen vacancies and their content in oxides can further improve the structural preservation of the catalyst during the reaction while maintaining activity.

In addition, the origin of defect sites from metal cations can also change the catalytic activity. Wei *et al*. [70] prepared a MnO$_2$ support containing Mn^{3+} vacancies through an electrochemical charge-discharge process. They supported Pt on Mn^{3+} vacancies by electrodeposition and further nucleated and grew Pt nanoclusters (Fig. 7g). Moreover, the calculated results (DOS) showed that Pt$_{AC}$-MnO$_2$ has an obvious peak between 0.8−2 eV, indicating the strong bonding of Pt and O orbitals, thus confirming the SMSI between Pt and the support (Fig. 7h). In addition, Pt$_{AC}$-MnO$_2$ had a lower water dissociation energy barrier (Fig. 7i), which further enhanced the H desorption rate, and SMSI also inhibited the further migration of Pt nanoclusters, resulting in good hydrogen evolution stability. Consequently, in the design of oxide-supported Pt catalysts for the HER, further control of vacancy defects and fine-tuning of the electronic structure are key strategies for improving the efficiency of electrocatalytic hydrogen evolution.
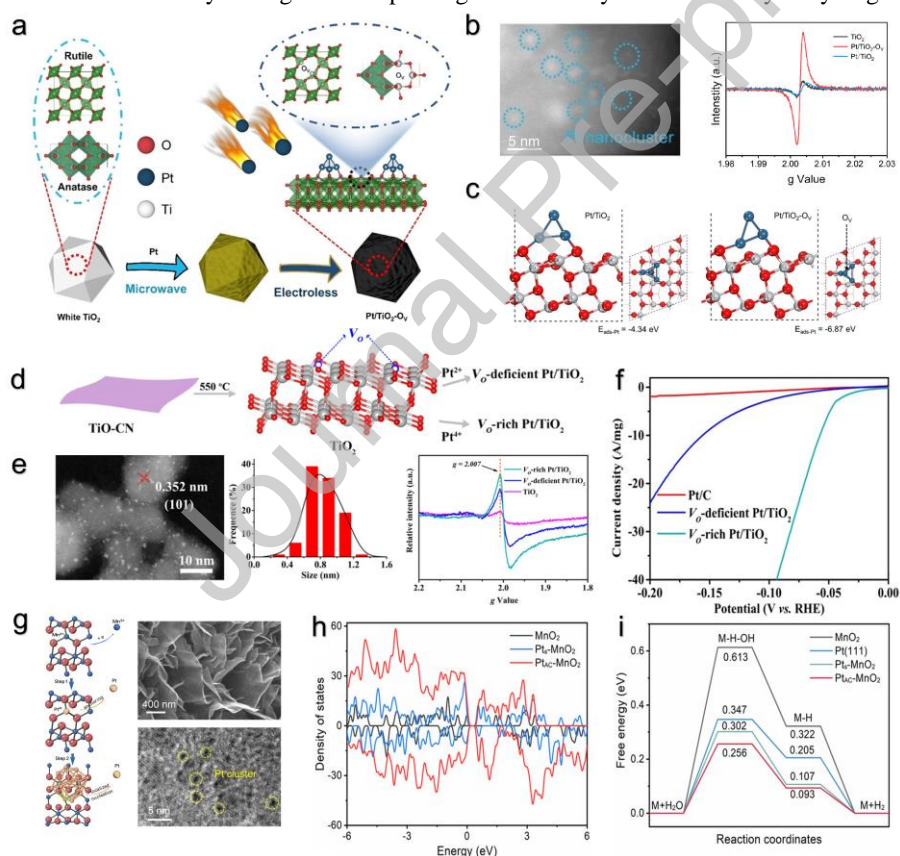

Fig. 7. (a) The schematic showing the synthesis method for Pt/TiO$_2$-O$_V$. (b) HAADF-STEM images of Pt/TiO$_2$-O$_V$ (left part) and EPR spectra of TiO$_2$, Pt/TiO$_2$-O$_V$ and Pt/TiO$_2$ (right part). (c) The adsorption energy of Pt onto TiO$_2$ (left part) and Pt/TiO$_2$-O$_V$ (right part). (a-c) Copied with permission [35]. Copyright 2023, Wiley-VCH. (d) A graphical representation of the synthesis process for V$_O$-deficient and V$_O$-rich Pt/TiO$_2$. (e) HAADF-STEM images and ESR spectra of V$_O$-rich Pt/TiO$_2$, the associated size distribution is shown in the middle. (f) The corresponding polarization curves in 0.5 mol/L H$_2$SO$_4$. (d-f) Copied with permission [85]. Copyright 2021, Wiley-VCH. (g) Diagram of Pt nucleation and growth process, SEM images (upper part) and TEM images (lower part) of V$_O$-rich Pt/TiO$_2$. (h) Calculated DOS of MnO$_2$, Pts-MnO$_2$, and Pt$_{AC}$-MnO$_2$. (i) The ΔG_{H*} of HER on the surface of MnO$_2$, Pt (111), Pts-MnO$_2$, and Pt$_{AC}$-MnO$_2$. (g-i) Copied with permission [70]. Copyright 2021, Wiley-VCH.

5.2 Pt nanocluster-based carbide electrocatalysts

Transition metal carbides (TMCs) represent a notable category of support material for electrocatalysts, distinguished by their exceptional mechanical stability, high electrical conductivity, resistance to poisoning, and structural stability in acidic environments

[89] n transfer between Pt and the TMC support owing to its electronic structure, which is akin to that of noble metals [91], which is conducive to the structural stability and high catalytic activity of the catalyst [92]. Therefore, rationally designing the morphology and structure of carbide supports and depositing metals to fully expose the binding sites are conducive to further taking into account the activity and stability of catalysts [76,93–96]. Wu *et al*. [94] prepared three-dimensional (3D) crumpled $Ti_3C_2T_x$ MXene supported sub-nanometer Pt nanoclusters (Pt/MXene) (Fig. 8a). Among them, not only was the overlapping of layered MXene suppressed (Fig. 8b), but the 3D structure also enabled full exposure of the Pt nanoclusters (Fig. 8c). Compared with the directly freeze-dried layered MXene ($F-Ti_3C_2T_x$), the spray-dried MXene ($S-Ti_3C_2T_x$) had a larger specific surface area, approximately 4 times that of $F-Ti_3C_2$ (Fig. 8b). Zhao *et al*. [96] designed a catalyst with snowflake-like Pt nanoclusters supported on MXene by adjusting the morphology and structure of the Pt metal (Figs. 8d and e). Pt nanoclusters have more exposed active sites due to their unique snowflake-like structure, and the co-regulation of Ti and F weakens the adsorption of active H^* on Pt (Fig. 8f), resulting in stronger catalytic properties for MXene/B-Pt. Yuan *et al*. [76] used a laser hybrid model to construct a combined catalytic and gas diffusion electrode ($Pt/Mo_2C-L/Mo$) (Fig. 8g). Interestingly, the substrate of the Mo_2C-L/Mo micropillar array contained an abundant hydrophilic surface area and a large specific surface area, which is conducive to better dispersion of the Pt nanoclusters. Such a structure endows the catalyst with excellent HER performance (10 mA/cm^2 for 21 mV) in acidic electrolyte (Fig. 8h). In addition, a proton exchange membrane water electrolyzer (PEMWE) prepared by spraying a cathode catalyst as $Pt/Mo_2C-L/Mo$ and an anode catalyst as TiO_2/Ti demonstrated robust stability in both acidic and pure water environments (Fig. 8i). Consequently, the efficient customization of the carbon support with a distinctive structure, aimed at augmenting the binding sites between the support and Pt nanocluster, can more effectively address both the hydrogen evolution activity and stability of the catalyst.
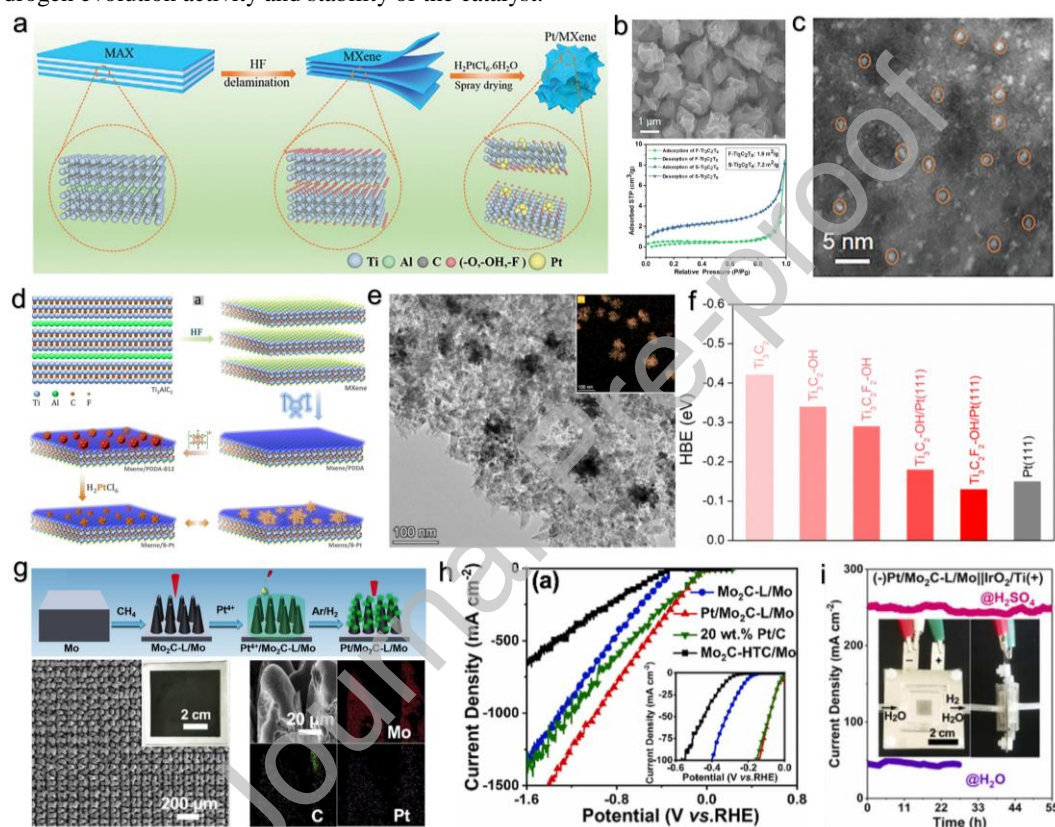

Fig. 8. (a) A schematic representation of the design of the Pt/MXene catalyst. (b) Corresponding SEM images and N_2 adsorption–desorption isotherm curves. (c) HAADF-STEM images for the synthesized Pt/MXene. (a-c) Copied with permission [94]. Copyright 2022, Wiley-VCH. (d) Schematic diagram of the preparation pathway of MXene/B-Pt. (e) TEM images of MXene/B-Pt. (Inset: the corresponding element mapping). (f) Hydrogen Adsorption energy of Ti_3C_2, Ti_3C_2-OH, $Ti_3C_2F_2$-OH, Ti_3C_2/Pt (111), $Ti_3C_2F_2$-OH/Pt (111) and Pt (111). (d-f) Copied with permission [96]. Copyright 2023, Royal Society of Chemistry. (g) Illustration of the laser synthetic process of $Pt/Mo_2C-L/Mo$ (upper part), SEM images (left part) and the corresponding element mapping (right part) of $Pt/Mo_2C-L/Mo$. (h) The linear sweep voltammetry (LSV) for different catalysts in 0.5 mol/L H_2SO_4 (inset was detail drawing). (i) Current-time curves (~ 2.10 V) of the assembled PEMWE devices in 0.5 mol/L H_2SO_4 and H_2O. (g-i) Copied with permission [76]. Copyright 2022, Elsevier.

5.3 Pt nanocluster-based hydroxide electrocatalysts

5.3.1 Interface interaction

Metal hydroxides represent a novel and significant class of inorganic functional materials, notable for their distinct structures and flexible, tunable chemical compositions. They have found widespread application in diverse areas, including biomedicine, photoluminescence, electrochemical energy storage and conversion technologies [97–101]. As electrocatalyst supports for hydrogen evolution, metal hydroxides can provide abundant edge sites to promote water dissociation and intermediate adsorption, which are helpful for the supported metal (Pt) to adsorb hydrogen intermediates, thereby promoting HER performance [102]. For example, Yang *et al*. [75] prepared Pt clusters on porous α-$Ni(OH)_2$ nanowires, referred to as $Pt_c/Ni(OH)_2$ (Fig. 9a). The porous structure of $Pt_c/Ni(OH)_2$ facilitated a substantial loading of Pt nanoclusters, achieving a high Pt loading of 4 wt%. XPS spectrum (Pt 4f) showed the coexistence of Pt^{2+} and Pt^0 in $Pt_c/Ni(OH)_2$. Interestingly, the chemical state of Ni(II) does not change significantly after the modification of atomic-scale Pt nanoclusters on $Pt_c/Ni(OH)_2$ (Fig. 9b). Upon evaluating their electrochemical characteristics, it was found that $Pt_c/Ni(OH)_2$ displayed the best polarization performance compared to Pt/C in alkaline media, while also maintaining robust stability. (Fig. 9c).

To further increase the loading and HER activity, layered double hydroxides (LDHs) are another type of commonly used supports. They possess unique features such as the variability of ions within their layers, the ability to exchange anions between layers, and a substantial reactive surface area, all of which contribute to their outstanding electrocatalytic performance in hydrogen evolution. Yan *et al*. [101] successfully synthesized functionalized NiFe LDH nanosheets incorporating Pt nanoclusters (~0.59 nm) through a straightforward hydrothermal method (Fig. 9d). The resulting catalyst featured highly dispersed Pt nanoclusters, exposing aan increased number of active sites. Notably, the catalyst demonstrated HER activity comparable to that of commercial Pt/C in alkaline electrolyte conditions, where the overpotential of 10 mA/cm^2 was only 28 mV (Fig. 9e). Hence, the direct interaction between the binding sites exposed by layered metal hydroxide and Pt nanoclusters proves advantageous in stabilizing the structure of Pt nanoclusters and enhancing the overall performance in hydrogen evolution.
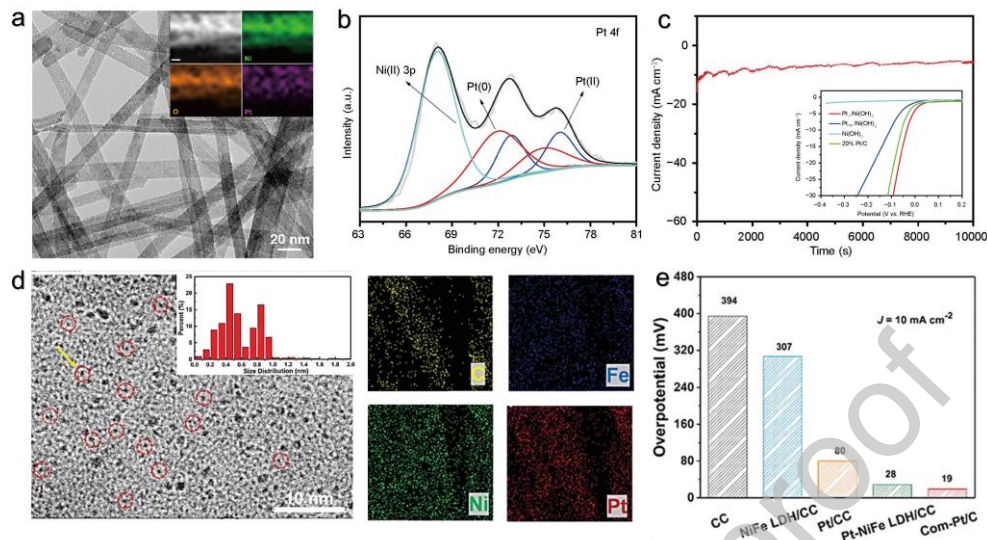

Fig. 9. (a) TEM and EDS analysis of the Ptc/Ni(OH)$_2$. (b) High-resolution Pt 4f XPS spectra of Ptc/Ni(OH)$_2$. (c) Chronoamperometric curve of Ptc/Ni(OH)$_2$ at an overpotential of 70 mV (inset was HER data of different catalysts in 0.1 mol/L KOH). (a-c) Copied with permission [75]. Copyright 2017, Science Press. (d) HRTEM image and EDS mapping (C, Fe, Ni, Pt) of Pt-NiFe LDH nanosheets. Inset shows the size distribution of the sub-nanoclusters. (e) Comparison of overpotential of different catalysts at 10 mA/cm^2. (d, e) Copied with permission [101]. Copyright 2019, American Chemical Society.

5.3.2 Defect design

The synthesis of LDH nanosheets, subjected to alkali etching that induced metal defects, resulted in a decrease in their thickness and led to the formation of a hierarchical structure with both microporous and mesoporous characteristics. This structural transformation enhanced the diffusion of hydrogen adsorption intermediates, consequently leading to an increased exposure density of active sites. This modification in structure proved to be advantageous for the overall catalytic process. [103,104]. For example, Yu *et al*. [103] successfully developed a NiFe layered double hydroxide nanosheet, incorporating some vacancy defects (Ni$_x$Fe LDHs), and supported sub-nanomer Pt clusters (NCs) using a straightforward electrodeposition technique, resulting in a Pt/Ni$_x$Fe LDH composite. Specifically, Pt-supported Ni$_x$Fe LDHs were prepared through the introduction of Pt and the removal of Zn (Figs. 10a and b). Upon comparing the XPS spectra, it was found that the Ni^{2+} content of the defect-type Pt/LDH composite significantly decreases, whereas the Ni^{3+} content increases, indicating that Ni^{2+} defects are generated. In addition, Pt/Ni$_x$Fe LDHs exhibited more zero-valent Pt signals, which indicates that Ni^{2+} defects promote more reduction of Pt ions (Fig. 10c). The synergistic interaction between the defective supports and Pt nanoclusters was found to decrease the adsorption of *H intermediates and promotes the HER performance. (Fig. 10d).

Feng *et al*. [104] further doped V on the Fe defects of NiFe LDH (Fig. 10e). The low electronegativity of V caused more charge to be transferred from V to Fe, changing the chemical environment of the adjacent Fe atoms (Fig. 10f). DFT calculations suggested that doping with V extends the Fe–O bond length in NiFeV LDH. Subsequent XPS analysis confirmed that the valence state of Fe in NiFeV LDH decreased. (Fig. 10g), and the outcome of this charge transfer enhances the self-reduction capabilities of the Pt nanoclusters on the support. Consequently, it was observed that the d-band center of Pt in Pt/NiFeV LDH shifted downward compared to that in Pt/NiFe LDH. This shift leads to a weaker adsorption capacity for H*. Moreover, the reduction in the d-band center of Ni atom was advantageous for facilitating the desorption of generated oxygen, thereby improving the HER activity of the catalyst (Fig. 10h). Therefore, optimizing the structure of metal ion defects by further regulating the in-layer ions of metal hydroxides is a key step in improving the HER activity of Pt-based hydroxide catalysts.
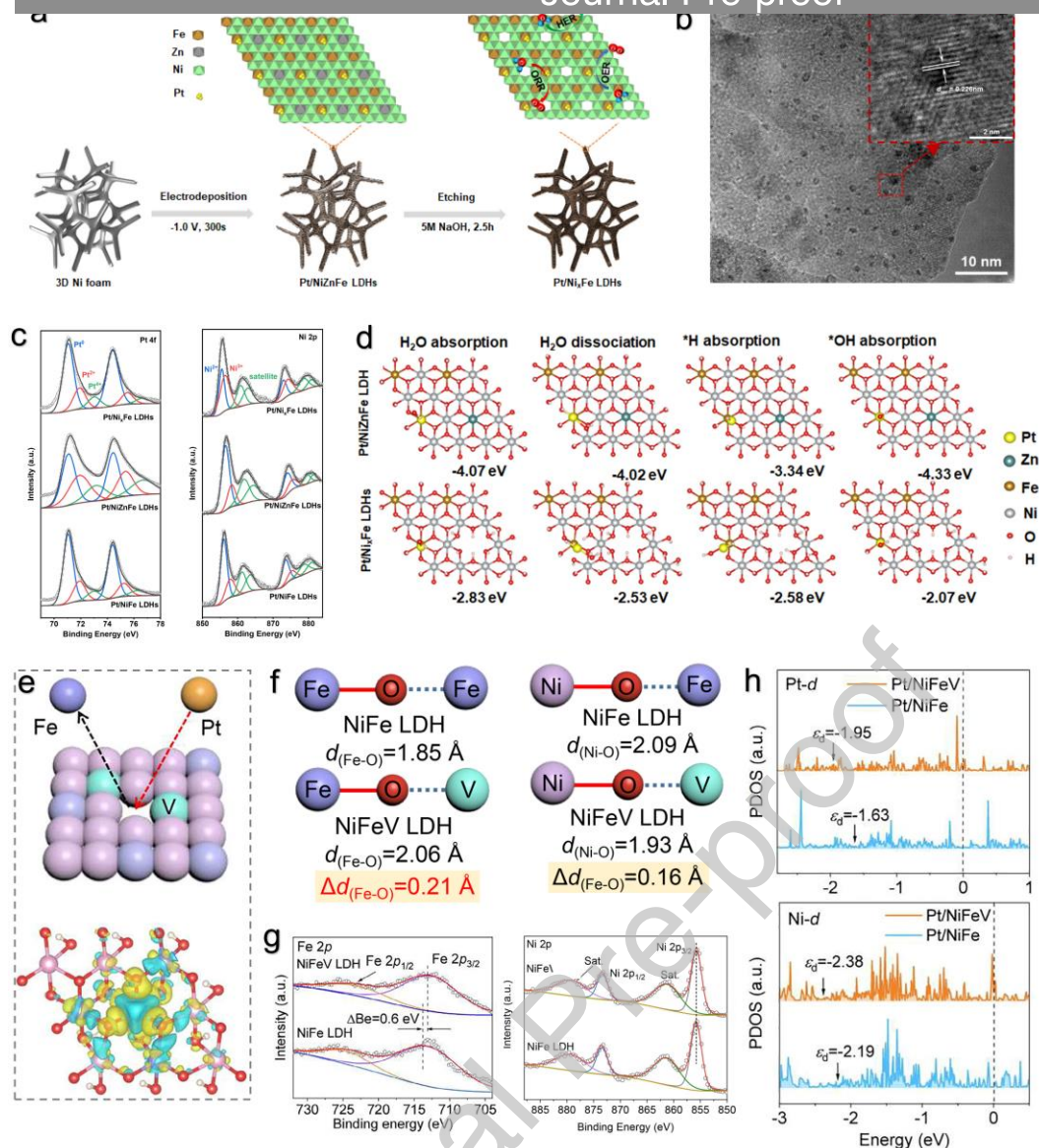
Fig. 10. (a) Diagram of the formation of Pt/Ni$_x$Fe LDHs. (b) TEM and HRTEM (inset) image of Pt/Ni$_x$Fe LDHs. (c) High-resolution XPS spectra (Ni 2p and Pt 4f) of different catalysts. (d) Optimized model structures of H$_2$O, H$_2$O dissociation, *H, and *OH adsorbed on Pt/Ni$_x$Fe LDHs and Pt/NiZnFe LDHs surfaces. (a-d) Copied with permission [103]. Copyright 2021, American Chemical Society. (e) A schematic representation of the synthesis process for Pt/NiFeV and its differential charge density. (f) The alteration in bond length resulting from the introduction of Vanadium (V) into the NiFe LDH. (g) Corresponding high-resolution XPS spectras. (h) PDOS of the 3d electron orbital for Pt atom (upper) and Ni atom (lower). (e-h) Copied with permission [104]. Copyright 2022, Elsevier.

5.4 Pt nanocluster-based carbon material electrocatalysts

5.4.1 Interface interaction

Carbon-based materials are considered attractive catalyst supports [29,105]. First, the graphite skeleton is highly conductive, facilitating charge transfer between the scaffold and the metal [106]. Second, the exposure of more efficient active sites is facilitated by a large specific surface area and high porosity. Furthermore, the electronic structure of the catalytic sites can be effectively modulated through SMSI or interfacial effects, which in turn significantly enhance the electrocatalytic performance [40,107–111]. Ma *et al.* [107] prepared Pt nanoclusters (0.5 wt%) on carbon nanotubes (CNTs) by photoreduction (Fig. 11a). Among them, to promote the reduction of PtCl$_6^{2-}$ and provide active sites, they used polydopamine (DPA) to modify the surface of CNTs. The XPS spectrum showed that the Pt catalyst with a size of 1.5 nm exhibited more Pt$^{\delta+}$ types (Fig. 11b). This result was mainly due to the transfer of charge from Pt to CNTs, which also confirmed the occurrence of SMSI between the Pt nanoclusters and the CNT support. In addition, such catalysts (1.5 nm Pt) exhibited optimal hydrogen evolution performance (Fig. 11c). Chen *et al.* [40] further anchored Pt nanoclusters on two-dimensional (2D) fullerene nanosheets (Fig. 11d). Specifically, matching of ultra-small Pt nanoclusters with larger lattice spacing fullerene nanosheets leads to strong confinement of the Pt nanoclusters, which emerges at the Pt/fullerene interface charge redistribution. Fig. 11e shows that the Pt 4f peak of Pt/C$_{60}$ was broader than that of pristine Pt nanoclusters (Pt NCs), indicating an increased content of Pt$^{\delta+}$ species and confirming charge transfer from Pt to the support. Interestingly, they compared the Pt 4f orbital binding energy of Pt with different mass loadings and found that when the mass loading of Pt nanoclusters increased to 1.1 μg/cm^2, the electronic binding energy of the Pt 4f orbital decreased to 71.4 eV (Fig. 11f). This finding further demonstrated that the interaction between Pt and C$_{60}$ was short-ranged, indicating that the catalytic performance of Pt clusters situated far from the Pt/C$_{60}$ interface was unaffected by the MSI.

To further confine the Pt nanoclusters, their migration and agglomeration were limited, and stability during the electrolytic hydrogen production process was ensured. Many researchers have focused on carbon sphere-type carriers [112–114]. This support has a larger accessible surface area and more nanopores to effectively confine Pt nanoclusters, which is more conducive to enhancing the

preservation of the catalyst structure in the electrolytic reaction. Fan *et al*. [108] constructed hollow graphene spheres (Pt/GHSs) with functionalized Pt nanoclusters (Fig. 11g). However, the obtained Pt/GHSs partially collapsed and failed to maintain a good spherical structure, which was likely to cause partial loss of effective active sites and a decrease in catalytic activity.

Therefore, Wan *et al*. [109] utilized tetrapropyl orthosilicate (TPOS) instead of TEOS as the Si source, reducing its hydrolysis and condensation behavior. The SiO_2 template was removed before the incorporation of the Pt source, resulting in mesoporous carbon spheres (HMCS), preventing the destruction of the catalyst (Pt_5/MHCS) structure by the etchant (Fig. 11h). Specifically, Pt clusters were uniformly confined on the surface of the HMCS (~0.77 nm). Compared with Pt/C, the catalyst has both remarkable catalytic activity and cycle stability (Fig. 11i), confirming the structural stability and high number of active sites of Pt_5/MHCS. Therefore, by designing the morphology of the carbon material and optimizing the MSI between the Pt nanoclusters and the support, it is possible to better design hydrogen evolution catalysts with excellent activity and stability.
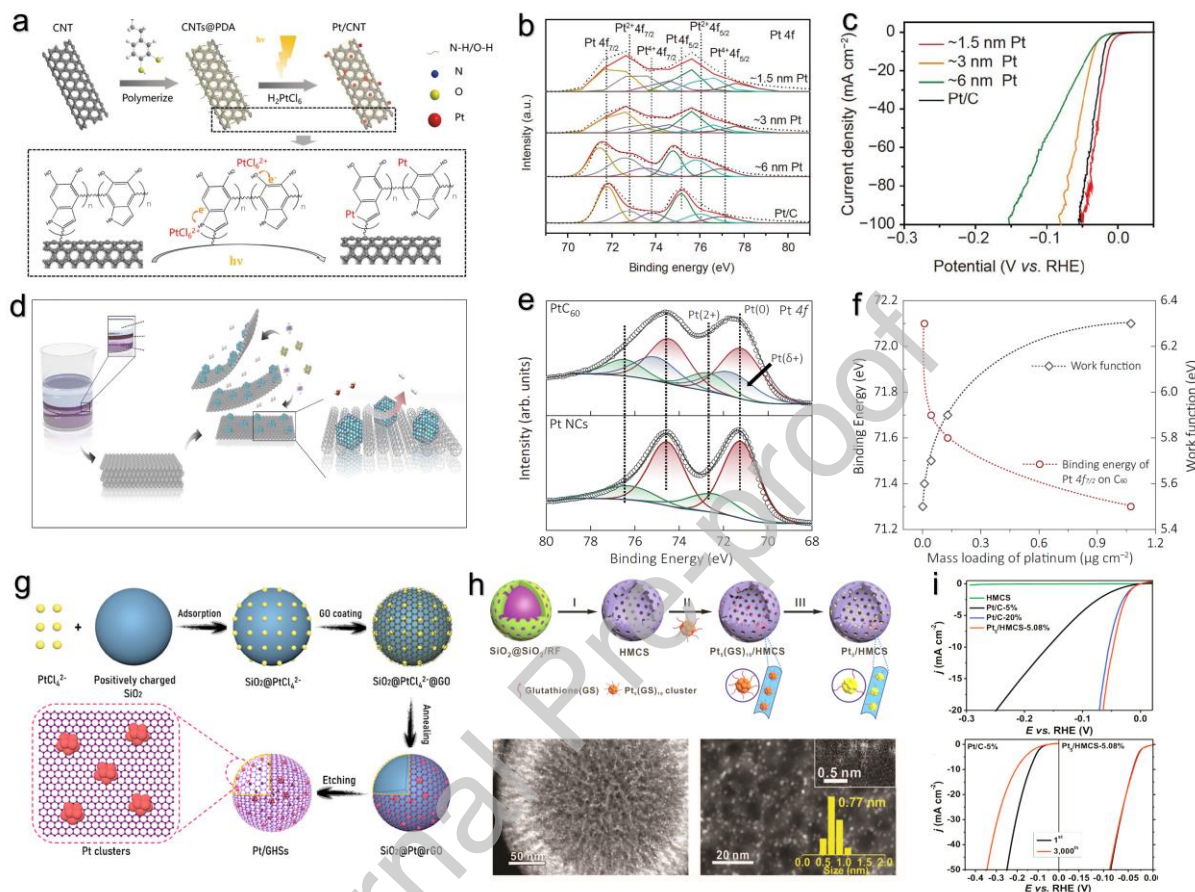

Fig. 11. (a) A schematic representation of the procedure used to design a Pt/CNTs through photoreduction. (b) High-resolution XPS spectra of the catalysts with difference metal sizes. (c) The polarization curves for different catalysts in 0.5 mol/L H_2SO_4. a-c) Copied with permission [107]. Copyright 2020, Science Press. (d) Schematic of the process of PtC_{60}. (e) High-resolution XPS spectra for PtC_{60} and Pt NCs. (f) The binding energy and work function variations based on the quantity of Pt deposited on the C_{60} film. (d-f) Copied with permission [40]. Copyright 2023, Nature Portfolio. (g) A schematic illustration depicting the synthesis process of Pt/GHSs. Copied with permission [108]. Copyright 2021, Elsevier. (h) A schematic diagram representing the synthesis of Pt_5/MHCS, accompanied by HAADF-STEM images, with an inset showing the size distribution of the Pt cluster. (i) A comparative analysis of the linear polarization curves and potential cycle stability of Pt_5/MHCS-5.08% with commercial catalysts. (h, i) Copied with permission [109]. Copyright 2020, Elsevier.

5.4.2 Defect design

Recently, it has been recognized that structural defects within the carbon framework can serve as effective active sites, rather than just modifying the supporting metal atoms [115,116]. Compared with normal hexagonal sites, defect sites with lower work functions and greater reducing abilities preferentially anchor high-priced Pt and promote its reduction, improving the number of active Pt atoms. In addition, the strong interaction between Pt and defective carbon supports effectively inhibits the agglomeration of Pt nanoclusters, enabling the realization of Pt catalysts with highly stable structures [117]. Bao *et al*. [116] employed a facile in situ electrochemical strategy to fabricate stable PGM clusters (Pt, Pd, and Au) supported on structural defects in carbon nanotubes (CNTs) (Fig. 12a). Specifically, the DFT results showed that the adsorption energy of Pt nanoclusters with vacancy defect structures (di- and mono-vacancies) on the support was the strongest, confirming the strong interaction between the carbon supports with vacancies and Pt nanoclusters (Fig. 12b). The carbon vacancies optimized the electron density of states, inhibited the migration and oxidation of Pt nanoclusters, and realized highly stable hydrogen evolution performance. Fig. 12c shows that the Pt/CNTs-ECR had the optimal hydrogen evolution activity, and the performance hardly changed after 10,000 potential cycles, reflecting the excellent durability of the catalyst.

Dai *et al*. [117] further studied the effect of the carbon defect content on the structure and performance of a catalyst. They adjusted the density of carbon defects by controlling the etching time of ammonia gas on graphene oxide and obtained Pt clusters supported by defect graphene (Pt-AC/DG) (Fig. 12d). A comparison of the Raman spectra (Fig. 12e) revealed that the support with the longest ammonia gas etching time (DG-45min) had the largest I_D/I_G value (1.28), indicating that its carbon defect density was the largest.

Fur... carbon defects anchor the Pt nanoclusters well and inhibit their migration. Interestingly, the Pt nanocluster catalyst with the smallest size exhibited better hydrogen evolution activity and stable electrolysis ability (Figs. 12g and h). The DFT results clarified that the binding energy of the Pt/DG structure model was much greater than that of Pt/PG (perfect graphene), reflecting the SMSI between Pt and the support (Fig. 12i). Therefore, adjusting the defect density of the carbon material substrate is a key step in improving the binding energy of Pt and support and adjusting the size of Pt, which has important research significance for promoting the development of hydrogen evolution catalysts with low-cost and highly stable structures.
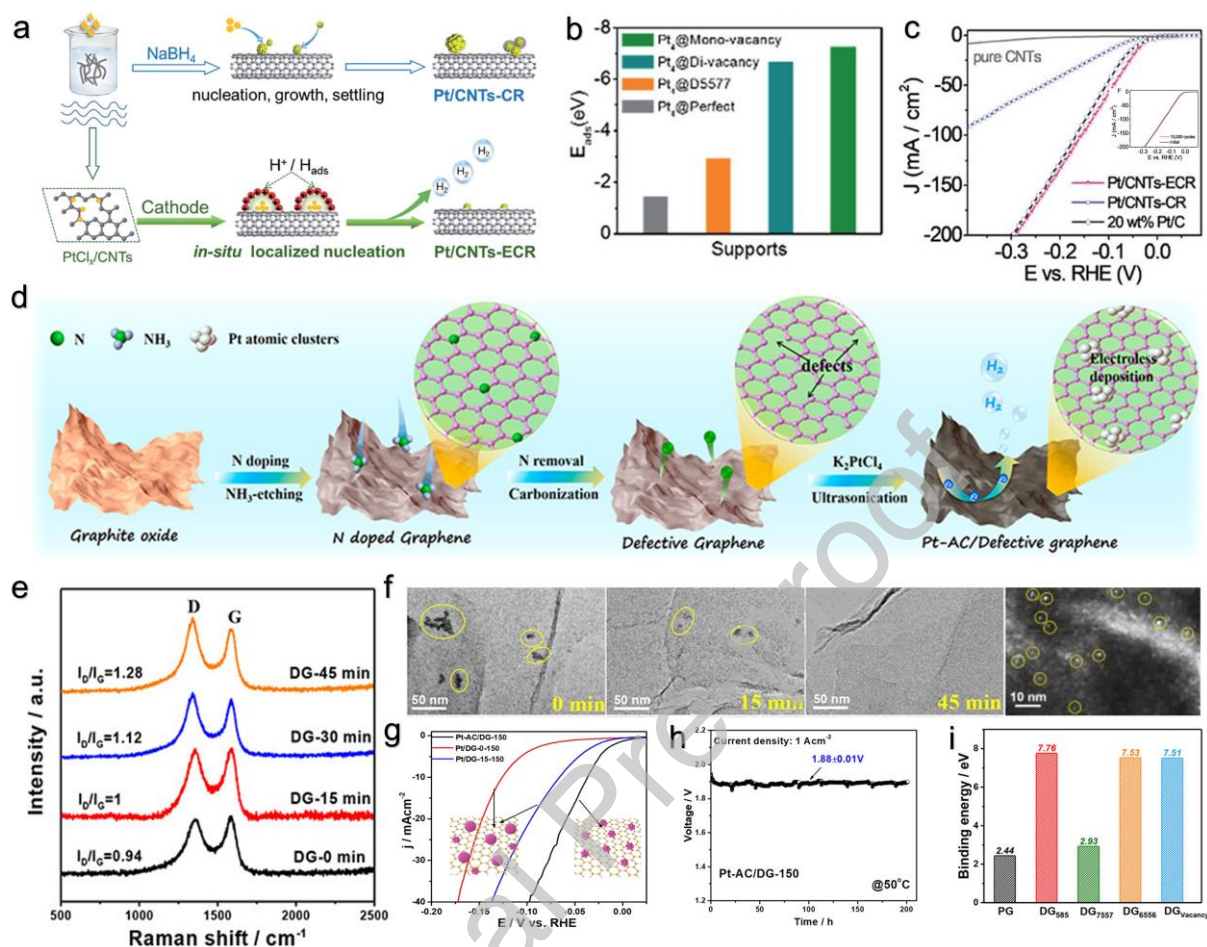

Fig. 12. (a) A diagram illustrating the preparation process for Pt/CNTs-ECR and Pt/CNTs-CR. (b) The adsorption energy of Pt_4 cluster absorbed on different catalysts. (c) Electrochemical behaviors of Pt/CNTs-ECR, Pt/CNTs-CR and 20 wt% Pt/C (inset was potential cycle stability of Pt/CNTs-ECR). (a-c) Copied with permission [116]. Copyright 2019, Royal Society of Chemistry. (d) A graphical representation of the process for preparing Pt-AC/DG. (e) Raman spectroscopy results for Nitrogen-doped Graphene (NG) following the removal of nitrogen. (f) TEM and HAADF-STEM images of Pt/DG with different etching time. (g) Comparison of HER performance on the Pt-AC/DG-150, Pt/DG-0-150 and Pt/DG-15-150 samples. h) Constant current density (1 A/cm²) test. (i) The binding energy for PG and different DGs after electroless deposition. (d-i) Copied with permission [117]. Copyright 2020, American Chemical Society.

5.4.3 Nonmetal doping

The surface functional groups and inherent defects of carbon supports can interact with active metals to provide dispersed catalytic sites. Crucially, the doping of heteroatoms can further refine the electronic structure at the catalytic site and modulate the MSI [29]. Han *et al.* [118] achieved the co-doping of N and P in carbon nanotubes (NP-CNTs) through nitriding and phosphating processes. They then supported Pt nanoclusters on these carbon nanotubes, resulting in the creation of a Pt/NP-CNTs catalyst (Fig. 13a), which was subsequently applied in water electrolysis for hydrogen evolution. Moreover, N-doped carbon with a fully porous structure can be formed by pyrolysis treatment of metal-organic frameworks (MOFs) [52,119,120]. Therefore, Chen *et al.* [120] further constructed nitrogen-doped carbon-constrained Pt nanoclusters derived from ZIF-8 on a continuously conducting carbon nanotube substrate (CTA@Pt@NCBs). (Fig. 13b). Among them, N-doped carbon arrays derived from porous MOFs can ancor more Pt nanoparticles and further inhibit Pt migration. From the XPS spectrum, it was found that the N 1s peaks mainly existed for graphitic N, N-5, and N-6 (Fig. 13c). Specifically, N-5 and N-6 with marginal active sites were more conducive to capturing Pt clusters, and Lewis acidic N-6 can effectively adjust the adsorption free energy and dynamic transfer process of intermediates at the interface (Pt-C) [121,122], thus generating special interactions between Pt and carbon nanotubes and promoting rapid hydrogen evolution reactions.

The introduction of N into the Pt/C catalyst alters the electronic structure of Pt and C [123,124], creating electron vacancies that are more likely to improve the heavy d-π effect of the Pt-C junction [125]. To further clarify the pivotal influence of N in platinum-supported carbon material catalysts and delve into the substantial d-π effect, Xiao *et al.* [126] combined electrospinning, carbonization, and directional displacement techniques to fabricate a catalyst comprising ultrafine Pt nanoparticles supported on nitrogen-doped porous carbon fiber (Pt@NDPCF) (Fig. 13d). Among these materials, nanostructured carbon fibers obtained by electrospinning can achieve effective electron transport and enhance structural stability. Here, fiber optic technology and the replacement of Zn nanoparticles by Pt nanoparticles jointly realized the N-enhanced heavy d-π effect. Specifically, unlike Pt/C and Pt black, the Pt $4f_{5/2}$ core energy level of Pt@NDPCF moved by 0.9 and 1.33 eV towards higher binding energies, respectively, in the XPS spectrum (Fig.

13e), confirming that Pt and NDPCF charge transfer between them and form a strong d-π effect. On the other hand, compared to that in Zn@NDPCF, the pyridine N in Pt@NDPCF was shifted by 0.3 eV in the direction of low binding energy. Furthermore, the DFT results again verified the experimental conclusion (Fig. 13f). In Pt@NDPCF, the number of outermost electrons on Pt atoms was less than that on N atoms, indicating that N atoms attract electrons from Pt atoms. The fewer electrons in the outermost shell indicate that the d orbital of Pt is more empty, which is more conducive to the adsorption of reactants and enhances catalytic activity. Therefore, Pt@NDPCF showed better hydrogen evolution performance than did commercial Pt/C (Fig. 13g). These findings underscore the importance of heteroatom doping, such as N and P doping, in modulating the interaction between platinum (Pt) and its supports. This doping strategy aids in fine-tuning the electronic structure of catalysts, resulting in the creation of exceptionally active catalytic materials. Therefore, it is imperative to delve deeper into the precise control of heteroatoms in the context of MSI regulation and to clarify the internal theoretical mechanisms of the remarkable catalytic activity exhibited by these catalysts.
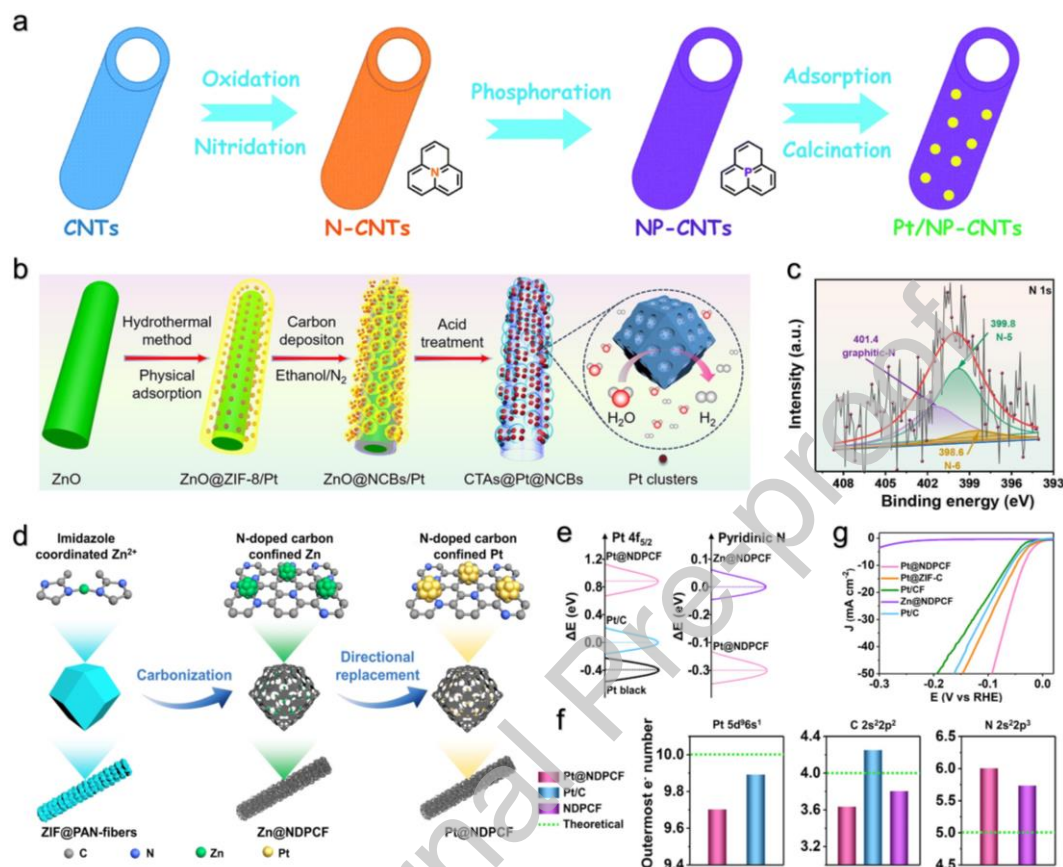

Fig. 13. (a) A diagram illustrating the preparation process of Pt/NP-CNT catalyst. Copied with permission [118]. Copyright 2022, Royal Society of Chemistry. (b) A schematic diagram depicting the synthesis process for CTAs@Pt@NCBs and (c) its high-resolution XPS spectra. (b, c) Copied with permission [120]. Copyright 2022, Elsevier. (d) Scheme illustration of the synthesis of Pt@NDPCF. (e) Pt $4f_{5/2}$ core levels for Pt@NDPCF and commercial Pt, on the right shows the Pyridinic N core level for Pt@NDPCF compared to Zn@NDPCF. (f) An analytical comparison detailing the quantity of valence electrons for Pt, C, and N atoms in the samples. (g) Polarization curves of Pt@NDPCF compared with the other catalysts in acid. (d-g) Copied with permission [126]. Copyright 2022, American Chemical Society.

5.4.4 Transition metal doping

Doping Pt-supported carbon materials with transition metals can effectively improve their intrinsic activity while reducing the use of PGMs. In these cases, heteroatom bond formation and ligand effects can be further manipulated to alter the chemical properties of multimetallic surfaces, leading to combined changes in the energy and width of the average surface d-band, resulting in optimized H* adsorption energies for enhanced HER activity [29]. In addition, carbon materials doped with one or more transition metals (Fe, Co, Ni, *etc*.) have shown excellent hydrogen evolution properties [127–130]. Therefore, doping with a suitable transition metal is highly important for improving MSI, optimizing the active sites of Pt, and promoting the hydrogen evolution activity of a catalyst. Peng *et al*. [72] prepared a catalyst (Ni-N-C/Pt) with Ni single-atom functionalized N-doped carbon nanosheets supporting Pt nanoclusters (Fig. 14a). Specifically, the migration of Pt was inhibited by the charge transfer between Ni-O-Pt, and single Ni atoms were stably confined within the carbon nanosheets by the strong combination of Ni-N-C. The catalyst with the optimal Ni addition (Ni-N-C-250/Pt) exhibited better performance than Pt/C under alkaline conditions. Among them, with only 100 mV of overpotential consumed, the normalization performance (*vs*. ECSA) of Ni-N-C-250/Pt reached 10.22 mA/cm^2 (Fig. 14b). Zhang *et al*. [69] controlled and optimized the catalytic activity of Pt through Co-Pt bimetallic nanoclusters supported by nitrogen-doped carbon nanosheets obtained through a spontaneous electrosubstitution reaction (redox reaction of Pt^{4+} and Co^0) (Fig. 14c). Among them, DFT results showed that hydrogen intermediates (H$_{ads}$) were more likely to combine with Pt, while OH− was more likely to combine with Co, which accelerated the water dissociation process in the Volmer step (Fig. 14d). Liu *et al*. [131] further used Zn-MOF as a sacrificial template (NC), introduced Mo and P, and obtained a hydrogen evolution catalyst (Pt/Mo, P@NC) (Fig. 14e). Interestingly, compared with only Mo- or P-doped catalysts

(Pt/ C

possessed more defect sites. This was mainly attributed to the co-regulatory effect of Mo and P, which created additional structural defects. In addition, more Pt metal signals were observed at the Pt 4f energy level for Pt/Mo/P@NC, which indicates that Mo and P jointly promote electron transport and change the MSI, which is beneficial for the generation of additional active sites on the catalyst (Fig. 14g).

With an adjustable pore structure, the metal types and coordination configurations of MOFs and their derived carbon nanomaterials can be further customized. Therefore, further optimization of the spatial confinement effect inside MOFs can achieve the preparation of a series of monatomic catalysts. [71,132]. In the case of synergistic catalysis involving cobalt (Co) sites within MOF, Lv *et al.* [127] selected single-Co-doped bimetallic (ZnCo) ZIF (Co SAs-ZIF-NC) as a substrate for Pt NPs (Fig. 14h). They isolated single-atom Co sites in porous nitrogen-doped carbon and anchored platinum nanoparticles, limiting their growth. In addition, Lei *et al.* [71] further employed MOF-derived carbon frameworks (Mn-SAs/NC) with isolated Mn atoms to anchor Pt nanoclusters (Fig. 14i). They found a redistributed charge density at the interface of the Pt and Mn-N_4 sites (Fig. 14j). Among them, compared with the M-N_4 site, the electron density around the Pt site significantly increases, indicating that the Pt site attracts electrons from the adjacent Mn-N_4 site, further reflecting the SMSI between the Pt and Mn-N_4 sites. These results also confirmed the excellent hydrogen evolution performance and stability of Mn-SAs/NC. Therefore, rationally adjusting the type and electronic structure of the second doped metal, as well as the coordination configuration and interaction form with Pt and carbon supports, will be of great help in screening hydrogen evolution catalysts with more effective active sites and highly stable structures.
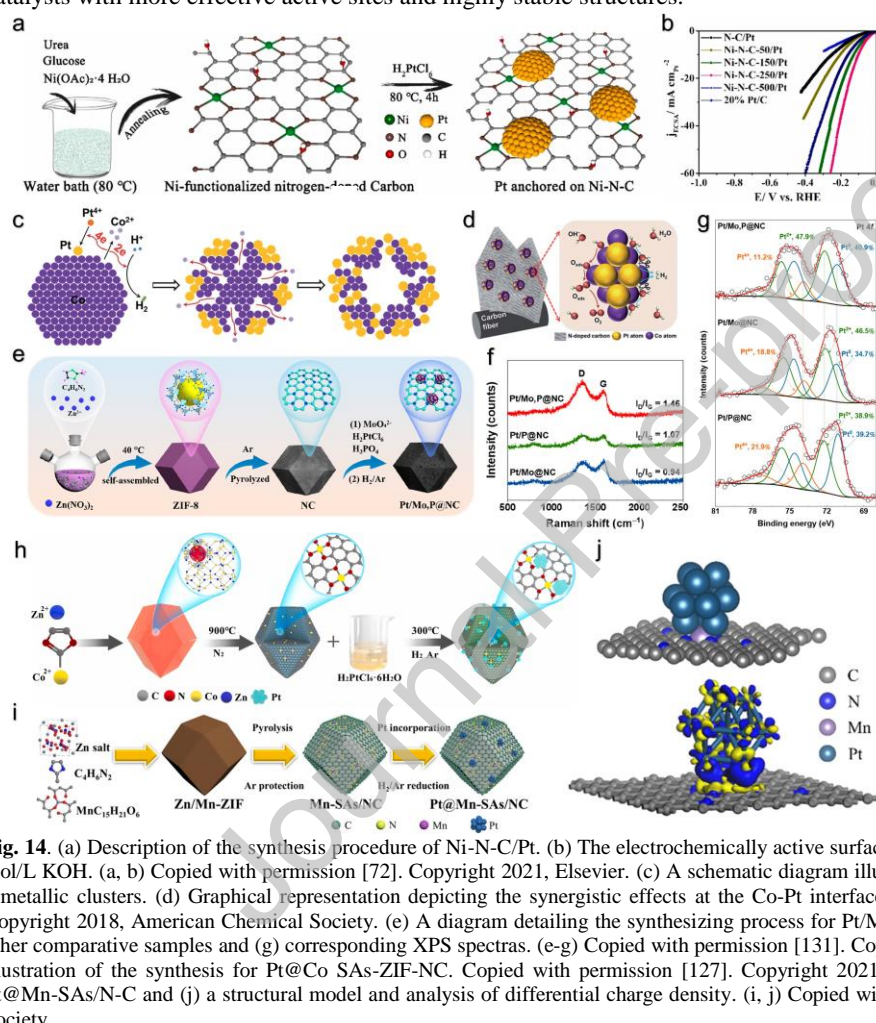

Fig. 14. (a) Description of the synthesis procedure of Ni-N-C/Pt. (b) The electrochemically active surface area (ECSA)-normalized HER polarization curves in 1 mol/L KOH. (a, b) Copied with permission [72]. Copyright 2021, Elsevier. (c) A schematic diagram illustrating the formation mechanism of open hollow Co–Pt bimetallic clusters. (d) Graphical representation depicting the synergistic effects at the Co-Pt interface in water splitting. (c, d) Copied with permission [69]. Copyright 2018, American Chemical Society. (e) A diagram detailing the synthesizing process for Pt/Mo,P@NC. (f) Raman spectra of Pt/Mo,P@NC alongside other comparative samples and (g) corresponding XPS spectras. (e-g) Copied with permission [131]. Copyright 2023, American Chemical Society. (h) Schematic illustration of the synthesis for Pt@Co SAs-ZIF-NC. Copied with permission [127]. Copyright 2021, Elsevier. (i) Schematic of the preparation process for Pt@Mn-SAs/N-C and (j) a structural model and analysis of differential charge density. (i, j) Copied with permission [71]. Copyright 2023, American Chemical Society.

5.5 Other supports

In addition to the supports already discussed, a wide array of other materials, including phosphides [133], sulfides [134,135], nitrides [136] and some amorphous supports [137], are suitable as catalyst supports for the HER. Tan *et al.* [133] grafted Pt nanoclusters on the edges of the Ni_2P/CoP nanosheets by electrodeposition (Fig. 15a). Through detailed finite element simulation analysis, it was found that the edge of the nanosheet promotes its attraction and reduction of Pt^{4+}, resulting in more active sites due to the local strong electric field. A further comparison of the adsorption energies showed that the adsorption energies of H* and H_2O* on Ni_2P/CoP-Pt were the weakest (Fig. 15b), confirming the strong interaction between the edge of the Ni_2P/CoP nanosheets and Pt, which results in better HER activity. Zhang *et al.* [137] synthesized an amorphous pentlandite $Fe_5Ni_4S_8$ (FNS) support with defects by high-temperature solid-state and ball milling methods and further supported Pt nanoclusters on the support by electrodeposition (Fig. 15c). The existence of a large number of defects in Pt-FNS composite catalysts endows Pt with good atomic dispersion and anchoring properties. Pt-FNS exhibited a lower d-band center than the pure FNS support (Fig. 15d), indicating that its adsorption to intermediates was weaker, which was more conducive to the desorption of products and improved the hydrogen evolution performance.
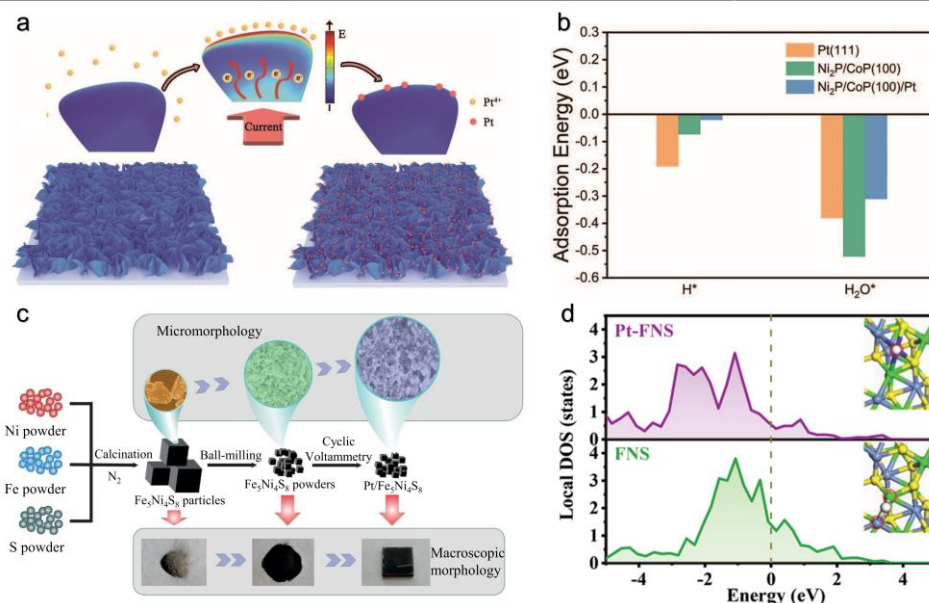
Fig. 15. (a) Illustration of Pt nanocrystal growth on the edge of a TMP nanosheet. (b) The adsorption energy for H* and H_2O* on Pt when a phosphate substrate is considered. (a, b) Copied with permission [133]. Copyright 2022, Elsevier. (c) Illustration of the synthetic route of the as-obtained samples. (d) Analysis of the DOS at hydrogen adsorption sites for FNS and Pt-FNS. (c, d) Copied with permission [137]. Copyright 2021, Elsevier.

6. Industrial application prospects and challenges of Pt nanocluster-based electrocatalysts

Presently, the application of water electrolysis as a method for hydrogen generation is increasingly recognized as a viable strategy for sustainable development. This technique has seen substantial progress and integration in various sectors, including renewable energy technologies and established traditional industries. The existing industrial water electrolysis devices are divided into four types: alkaline water electrolyzer (AWE), anion exchange membrane water electrolyzer (AEMWE), proton exchange membrane water electrolyzer (PEMWE), and high-temperature solid oxide electrolysis cell (SOEC) (Fig. 16a) [138,139]. Among them, the AWE system boasts the highest technology readiness level (TRL) of 6-8, offering numerous advantages such as cost-effectiveness and stable operation. However, their large-scale applications are limited by certain drawbacks, including low H_2 purity, significant ohmic losses, and sluggish reaction kinetics at high pH values [140,141]. While emerging AEMWE technology utilizes a low-concentration alkaline solution as the electrolyte, this technique remains in the nascent stages of development. Currently, it holds TRL values of 4-6. SOEC, another commercially promising technology, has a high conversion efficiency of 90% [142]. However, since SOECs usually operate at 700-1000°C, which presents significant challenges in terms of thermomechanical stability and electrochemical degradation. These issues pose considerable obstacles in advancing SOEC technology beyond the laboratory stage. Consequently, SOECs are currently classified with TRL values of 4-6. Compared with these systems, PEMWE has a higher TRL value of 6-8, and the use of PEM and a low pH environment in these systems not only enhances their activity but also contributes to increased safety. As a result, PEMWE has progressed beyond the experimental phase and entered commercialization, reflecting its viability and reliability in practical applications [143,144]. Table 2 presents a comparison of the performance metrics for four distinct types of water electrolyzers, providing a detailed overview of their respective capabilities and efficiencies for industrial applications [40,110,145-153].

Table 2
Comparison of the performance among different water electrolysis devices.

Device	Electrode area (cm²)	Current density (mA/cm²)	Performance (Voltage-V/Stability-h)	Temperature (°C)	Ref.
AWE	5	10	1.5/24	80	[145]
	25	500	1.84/250	80	[146]
	2	1000	1.87/20	60	[147]
AEMWE	5	270	2/100	25	[148]
	1	1000	2.01/20	60	[40]
	1	1000	1.98/500	25	[149]
	2	1000	1.74/48	80	[110]
PEMWE	1	100	1.61/500	25	[150]
	4	1000	/ /300	650	[151]
SOEC	0.5	500	1.1/300	750	[152]
	10	500	1.1/1000	800	[153]

Liu *et al*. [110] developed a Pt nanocluster electrocatalyst (SL-Pt) supported on an XC-72 carrier, and the PEMWE assembled with the anode IrO_2 catalyst had a potential of only 1.74 V when running at 1 A/cm², which was much lower than the potential of Pt/C (1.95V). The PEMWE assembled with SL-Pt is capable of continuous operation for 48 h at 1 A/cm² (Fig. 16b). In addition, the PtC_{60} catalyst designed by Chen *et al*. [40] can be applied to AEMWE, and it can stably produce hydrogen by electrolysis for more than 20 h under working conditions of 1 A/cm² (Fig. 16c). These Pt nanocluster-based hydrogen evolution catalysts all show impressive prospects for industrial applications. Nonetheless, the demanding conditions prevalent in operational settings necessitate that catalysts exhibit enhanced resilience [144]. A severe electrochemical reaction at a high current density leads to a sharp increase in hydrogen production, and the outside of the catalyst is likely to be overlaid by a bubble layer, which hinders the electrochemical reaction [154,155]. Therefore,

the [...] More seriously, the interfacial adhesion between the catalyst electrode and hydrogen bubbles causes part of the catalyst to peel off with the bubbles. Compared with the interface adhesion between the catalyst electrode and hydrogen bubbles, once the interface adhesion between the catalyst electrode and carrier is weaker, the peeling will be more serious, resulting in decreased stability. Hence, it is essential to further refine the MSI to enhance the mechanical stability of catalysts. In addition, the high cost of membrane electrode assembly (MEA) also greatly limits the industrial development of Pt nanocluster-based catalysts [156]. Therefore, in the future, researchers should strengthen the design of catalysts, membrane electrodes and structures in water electrolysers. By adjusting the materials and manufacturing processes, reducing cost expenditures, improving conversion efficiency, and reducing the gap between the performance of water electrolysers reported in the literature and actual industrial applications.
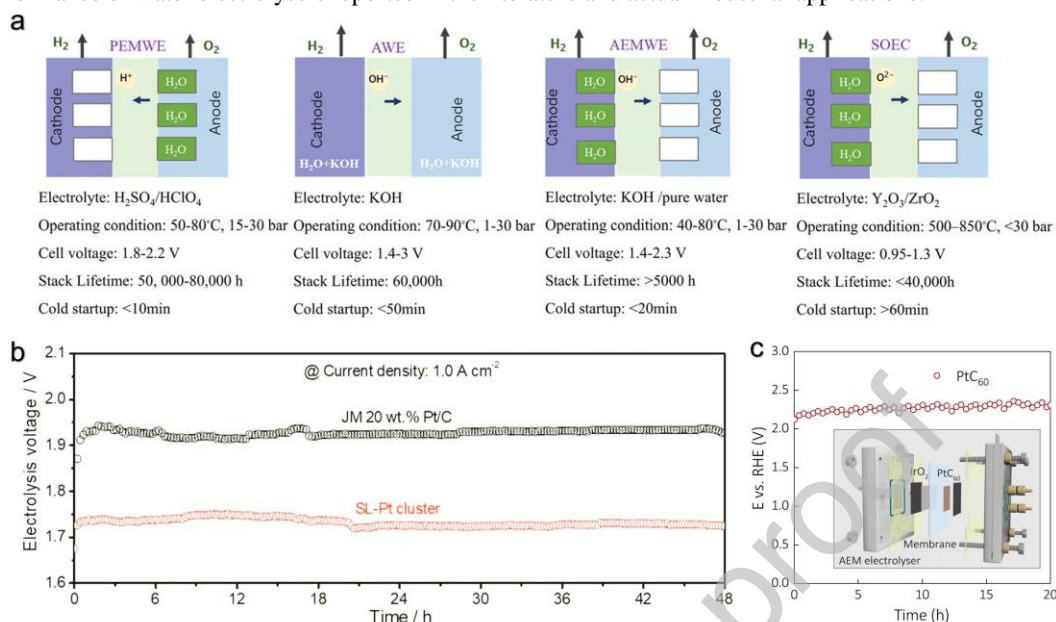

Fig. 16. (a) A schematic representation depicting the configuration of a water electrolyzer. Copied with permission [138]. Copyright 2022, Royal Society of Chemistry. (b) Stability test of SL-Pt in a PEMWE operating at 80 °C. Copied with permission [110]. Copyright 2022, Elsevier. (c) Chronopotentiometric curves of the AEM electrolyzer at 1 A/cm² (~60 °C). Copied with permission [40]. Copyright 2023, Nature Portfolio.

7 Summary and outlook

The large surface area, unique electronic characteristics, and strong substrate coupling make Pt nanoclusters a key area of interest in hydrogen production through water electrolysis. By investigating the underlying mechanisms of hydrogen evolution, tailoring various catalyst supports, fine-tuning the structural imperfections in these supports, and optimizing the interactions between the Pt nanoclusters and their supports, it is possible to engineer hydrogen evolution catalysts that exhibit both high catalytic activity and stability. Consequently, this manuscript offers a comprehensive review of the mechanisms underlying hydrogen evolution in Pt-based nanocluster catalysts. The primary kinetic steps involved are categorized into two main pathways: the Volmer-Tafel and Volmer-Heyrovsky mechanisms. This paper further elucidates the basic relation of optimizing the activity by regulating the electronic morphology of catalysts. Following this, the MSI of Pt nanocluster-based hydrogen evolution catalysts are detailed. Characterization techniques such as XPS, XAFS, Bader charge analysis, and d-band theory are employed to reveal the nature and form of the interactions between the Pt nanoclusters and their supports. Subsequently, the paper delves into the coupling strategies between Pt nanoclusters and various types of supports, including oxides, carbides, hydroxides, and carbon-based materials. This study also provides a detailed summary of the mechanisms related to the electronic structure that validate the source of catalyst activity. Specifically, for transition metal compounds, two primary methods are employed: direct loading of Pt nanoclusters onto the support and post-treatment of both the support and the Pt nanoclusters. The former technique maintains the shape and phase structure of the support and protects the metal active center, while the latter offers an additional layer of flexibility for optimizing the electronic structure of the metal center through the introduction of vacancies. In the realm of carbon-based supports, there is a greater possibility for post-processing modifications, encompassing aspects such as morphological control, structural defect engineering, and the incorporation of heteroatoms, which may include both non-metal and metal ions. These manipulations aim to precisely refine the electronic structure of the catalyst and ensure the stable anchoring of active metal sites. Table 3 compares the hydrogen evolution properties of Pt nanoclusters on different supports. While substantial progress has been made in the design and enhancement of catalysts based on Pt nanoclusters for hydrogen evolution, considerable challenges remain in meeting the performance criteria requisite for industrial-scale water electrolysis. Consequently, several recommendations are proposed to guide future research endeavors in this domain.

Table 3
Comparison of the HER properties of Pt nanocluster catalysts supported by different carriers.

Supports	Catalysts	Electorlyte	Current density (mA/cm²)	Overpotential (mV)	Stability (h)	Ref.
Metal oxides	F-SnO₂@Pt	0.5 mol/L H₂SO₄	10	42	60	[84]
	PtOx/TiO₂	0.5 mol/L H₂SO₄	10	121	/	[83]
	Pt-SL/TiO₂	1 mol/L KOH	5	170	/	[81]
	Pt/WO₃	0.5 mol/L H₂SO₄	10	8	65	[86]
	Pt/TiO₂-Oᵥ	0.5 mol/L H₂SO₄	10	18	20	[35]
	Pt Cs/MoO₂ NSs-L	0.5 mol/L H₂SO₄	10	47	12	[82]
	VO-rich Pt/TiO₂	0.5 mol/L H₂SO₄	/	/	24	[85]

	Catalyst	Electrolyte				Ref.
	PtAC-MnO$_2$	1 mol/L KOH	100	47	3.5	[70]
Metal carbides	MXene/B-Pt	1 mol/L KOH	10	14	100	[96]
	Pt/Mo$_2$C-L/Mo	0.5 mol/L H$_2$SO$_4$	10	21	100	[76]
	Pt/MXene	0.5 mol/L H$_2$SO$_4$	10	34	3	[94]
	MXene@Pt/SWCNTs	0.5 mol/L H$_2$SO$_4$	10	62	800	[93]
Metal hydroxides	Pt–NiFe LDH/CC	1 mol/L KOH	10	28	10	[101]
	Ptc/Ni(OH)$_2$	1 mol/L KOH	10	32	3	[75]
	Pt/NixFe LDHs	1 mol/L KOH	10	/	45	[103]
	Pt/NiFeV	1 mol/L KOH	10	19	10	[104]
Carbon materials	Pt NCs/rGO	0.5 mol/L H$_2$SO$_4$	10	67	/	[111]
	Pt/CNTs	0.5 mol/L H$_2$SO$_4$	10	13	/	[92]
	Pt-Co/NC	0.5 mol/L H$_2$SO$_4$	10	50	120	[74]
	Pt/GHSs	1 mol/L KOH	10	27	10	[108]
	Pt$_5$/HMCS	0.5 mol/L H$_2$SO$_4$	10	20.7	5.6	[109]
	PtC60	1 mol/L KOH	10	24.3	20	[40]
	Pt-AC/DG	0.1 mol/L HClO$_4$	10	21	200	[117]
	Pt/CNTs-ECR	0.5 mol/L H$_2$SO$_4$	10	24	30	[116]
	Co$_4$Pt	1 mol/L KOH	10	6.9	24	[130]
	Pt/Mo,P@NC	1 mol/L KOH	10	23.4	3	[131]
	Ni–N–C–250/Pt	1 mol/L KOH	10	100	10	[72]
	Pt@Co SAs-ZIF-NC	0.5 mol/L H$_2$SO$_4$	10	27	11	[127]
	Pt@NDPCF	0.1 mol/L HClO$_4$	10	24	/	[126]
	Pt@Mn-SAs/NC	0.5 mol/L H$_2$SO$_4$	10	25	25	[71]
	Pt/SnO$_2$@NPC-300	0.5 mol/L H$_2$SO$_4$	10	11.7	15	[129]
	CTAs@Pt@NCBs	0.5 mol/L H$_2$SO$_4$	10	27.42	60	[120]
Other supports	Pt-MoS$_2$	0.5 mol/L H$_2$SO$_4$	10	67.4	24	[134]
	1.5Pt@Ni$_3$N-360	0.1 mol/L KOH	10	71	/	[136]
	Bm-5d-Pt	0.5 mol/L H$_2$SO$_4$	10	30	24	[137]
	Ni$_2$P/CoP-Pt	1 mol/L KOH	10	44.5	80	[133]

(1) By integrating a diverse array of experimental characterization techniques with computational calculations, the source of activity and reaction mechanism can be explained more clearly. This multi-faceted approach can be manifested through various aspects of the catalytic process, including changes in adsorption intermediates, kinetic pathways, and the evolution of Pt nanoclusters throughout the reaction. Employing a broad spectrum of experimental methods not only enriches the dataset but also provides a more nuanced understanding of the entire catalytic process. This holistic methodology serves to elucidate the reaction pathways with greater clarity, thereby contributing to the optimization of catalyst design and performance [40,85,155].

(2) A comprehensive understanding of MSI is pivotal for elucidating both their electronic structure and catalytic performance. To this end, advanced experimental characterization (XPS, UPS, XAFS, *etc.*) and theoretical calculation methods were used. These methodologies accurately determine the nature and extent of MSI. Specifically, they provide insights into the directionality of charge transfer between the metal and the support, thereby offering a clearer understanding of the origins of the catalyst's activity and stability.

By systematically investigating these interactions, researchers can not only identify the key factors that influence the electronic properties of Pt nanoclusters but also shed light on how these properties correlate with catalytic performance. This, in turn, enables the development of more effective and durable catalysts by optimizing these interactions. Understanding the charge transfer mechanisms can also reveal the conditions under which the catalyst remains stable, thereby providing a basis for the development of next-generation hydrogen evolution catalysts with enhanced performance and longevity. Therefore, a detailed exploration of these interactions is not merely an academic exercise but also a critical step in the advancement of Pt nanocluster-based catalysts for practical applications [39,41,157].

(3) In the pursuit of sustainable, long-term hydrogen production via electrolysis, it is imperative to consider factors beyond merely the performance of the catalyst. One such critical factor is the durability of the whole electrode. Over extended periods of operation, electrodes are susceptible to corrosion and degradation, phenomena that can adversely affect their conductivity. This, in turn, escalates the energy costs associated with the electrolytic process, thereby underscoring the importance of electrode longevity as a determinant of the electrolyzer's operational lifespan. Additionally, the assembly methodology of the water electrolyzer itself warrants attention. Factors such as the coating technique for the catalyst, often achieved by spraying processes, and the choice of electrolyte can significantly influence the internal resistance of the entire system. It is worth noting that research at the laboratory stage often lacks experiential insights that are integral to industrial-scale water electrolysis systems. This gap in knowledge can result in suboptimal designs that are not fully attuned to the complexities of industrial applications. Consequently, researchers should aim to minimize problems attributable to these external conditions. This could involve the development of more corrosion-resistant electrode materials, optimization of catalyst coating techniques, or exploration of alternative electrolytes that offer lower internal resistance. By addressing these multifaceted challenges, the scientific community can make meaningful progress toward the realization of efficient and cost-effective hydrogen production systems [139,158,159].

(4) Finally, the catalysts must be amenable to rapid and continuous large-scale production, ensuring that they can be manufactured in quantities sufficient to meet industrial demands. Additionally, the fabrication process must allow for meticulous control over the effective sites outside the catalyst, thereby enabling precise tuning of the electrocatalytic performance. In summary, the development of Pt nanocluster-based catalysts with industrial stability is a complex undertaking that requires a harmonious blend of scalable manufacturing processes, precise control over active site characteristics, and rigorous performance validation under conditions mimicking industrial operations.

Declaration of competing interest

The authors declare no competing financial interests.

References

[1] J.P. Gattuso, A. Magnan, R. Billé, et al., Science 349 (2015) acc4722.
[2] C. Wei, R.R. Rao, J. Peng, et al., Adv. Mater. 31 (2019) 1806296.
[3] T. Takata, J. Jiang, Y. Sakata, et al., Nature 581 (2020) 411–414.
[4] X. Tan, J. Nielsen, Chem. Soc. Rev. 51 (2022) 4763–4785.
[5] J. Li, X. Liu, H. Wang, et al., Chin. Chem. Lett. 35 (2024) 108596.
[6] G. Palmer, Nat. Energy. 4 (2019) 538–539.
[7] X. Liu, J. He, S. Zhao, et al., Nat. Commun. 9 (2018) 4365.
[8] S. Chandrasekaran, L. Yao, L. Deng, et al., Chem. Soc. Rev. 48 (2019) 4178–4280.
[9] M.S. Zantye, A. Gandhi, Y. Wang, et al., Energy Environ. Sci. 15 (2022) 4119–4136.
[10] L. Wang, S. Nitopi, A.B. Wong, et al., Nat. Catal. 2 (2019) 702–708.
[11] H.L. Long, H.J. Peng, Chin. Chem. Lett. 34 (2023) 108033.
[12] J. Yu, W. Yu, B. Chang, et al., Chin. Chem. Lett. 33 (2022) 3231–3235.
[13] I. Staffell, D. Scamman, A. Velazquez Abad, Energy Environ. Sci. 12 (2019) 463–491.
[14] S. Chu, A. Majumdar, Nature 488 (2012) 294–303.
[15] B. Zhou, R. Gao, J.J. Zou, et al., Small 18 (2022) 2202336.
[16] J. Zhang, G. Chen, K. Müllen, Adv. Mater. 30 (2018) 1800528.
[17] X. Zhao, M. Chen, D. Wang, et al., Chin. Chem. Lett. (2023) 109327. doi: 10.1016/j.cclet.2023.109327.
[18] B. Guido, Scalable electrolytic systems for renewable hydrogen production: cooperative research and development final report. CRADA number CRD-18-747. Golden, CO (United States): National Renewable Energy Laboratory. NREL/TP-5900-76136.
[19] K. Christopher, R. Dimitrios, Energy Environ. Sci. 5 (2012) 6640–6651.
[20] T.S. Teitsworth, D.J. Hill, S.R. Litvin, et al., Nature 614 (2023) 270–274.
[21] T. Wang, L. Tao, X. Zhu, et al., Nat. Catal. 5 (2022) 66–73.
[22] X. Lu, S. Xie, H. Yang, et al., Chem. Soc. Rev. 43 (2014) 7581–7593.
[23] L. Wang, L. Duan, Y. Wang, et al., Chem. Commun. 50 (2014) 12947–12950.
[24] L. Wang, L. Duan, B. Stewart, et al., J. Am. Chem. Soc. 134 (2012) 18868–18880.
[25] Y. Gao, X. Ding, J. Liu, et al., J. Am. Chem. Soc. 135 (2013) 4219–4222.
[26] Y. Ma, H. Qu, W. Wang, et al., Chin. Chem. Lett. 35 (2024) 108352.
[27] J. Wang, W. Cui, Q. Liu, et al., Adv. Mater. 28 (2016) 215–230.
[28] H. Liu, N. Agrawal, A. Ganguly, et al., Energy Environ. Sci. 15 (2022) 4175–4189.
[29] Y. Liu, Q. Wang, J. Zhang, et al., Adv. Energy Mater. 12 (2022) 2200928.
[30] J. Ding, H. Yang, S. Zhang, et al., Small 18 (2022) 2204524.
[31] X. Zou, Y. Zhang, Chem. Soc. Rev. 44 (2015) 5148–5180.
[32] H. Yu, B. Yi, Chin. J. Eng. Sci. 20 (2018) 58.
[33] C. Zhang, H. Wang, H. Yu, et al., Adv. Energy Mater. 12 (2022) 2200875.
[34] D. Liu, X. Li, S. Chen, et al., Nat. Energy 4 (2019) 512–518.
[35] Z. Wu, P. Yang, Q. Li, et al., Angew. Chem. Int. Ed. 62 (2023) 2300406.
[36] R.C. Baetzold, J. Catal. 29 (1973) 129-137.
[37] J. Zhang, Y. Zhao, X. Guo, et al., Nat. Catal. 1 (2018) 985–992.
[38] Q. Dong, S. Ma, J. Zhu, et al., Adv. Funct. Mater. 33 (2023) 2210665.
[39] Y. Lykhach, S.M. Kozlov, T. Skála, et al., Nat. Mater. 15 (2016) 284–288.
[40] J. Chen, M. Aliasgar, F.B. Zamudio, et al., Nat. Commun. 14 (2023) 1711.
[41] Q.Q. Yan, D.X. Wu, S.Q. Chu, et al., Nat. Commun. 10 (2019) 4977.
[42] S.J. Tauster, S.C. Fung, R.L. Garten, J. Am. Chem. Soc. 100 (1978) 170–175.
[43] A. Bruix, J.A. Rodriguez, P.J. Ramírez, et al., J. Am. Chem. Soc. 134 (2012) 8968–8974.
[44] J. Wang, H. Zhang, X. Wang, Small Methods 1 (2017) 1700118.
[45] A.P. Murthy, J. Madhavan, K. Murugan, J. Power Sources 398 (2018) 9–26.
[46] Z.W. Seh, J. Kibsgaard, C.F. Dickens, et al., Science 355 (2017) eaad4998.
[47] Q. Gao, W. Zhang, Z. Shi, et al., Adv. Mater. 31 (2019) 1802880.
[48] C. Li, J.B. Baek, ACS Omega 5 (2020) 31–40.
[49] B.E. Conway, G. Jerkiewicz, Electrochim. Acta 45 (2000) 4075-4083.
[50] E. Skúlason, V. Tripkovic, M.E. Björketun, et al., J. Phys. Chem. C 114 (2010) 18182–18197.
[51] Y. Song, B. Xu, T. Liao, et al., Small 17 (2021) 2002240.
[52] X.F. Lu, B.Y. Xia, S.-Q. Zang, et al., Angew. Chem. Int. Ed. 59 (2020) 4634–4650.
[53] W. Wang, W. Geng, L. Zhang, et al., Small 19 (2023) 2206808.
[54] D. Wang, D. Jiao, M. Gong, Appl. Catal. B 325 (2023) 122331.
[55] Q. Wang, C.Q. Xu, W. Liu, et al., Nat. Commun. 11 (2020) 4246.
[56] W. Cao, Y. Xu, Z. Wang, J. Electrochem. Soc. 167 (2020) 104511.
[57] P.P. Edwards, J.M. Thomas, Angew. Chem. Int. Ed. 46 (2007) 5480–5486.
[58] J. Greeley, J.K. Nørskov, M. Mavrikakis, Annu. Rev. Phys. Chem. 53 (2002) 319–348.
[59] H. Shen, X. Tang, Q. Wu, et al., ACS Nanosci. Au 2 (2022) 520–526.
[60] J.H. Huang, L.Y. Liu, Z.Y. Wang, et al., ACS Nano 16 (2022) 18789–18794.
[61] M.A. Abbas, M. Jeon, J.H. Bang, Phys. Chem. C 126 (2022) 16928–16942.
[62] P. Gruene, D.M. Rayner, B. Redlich, et al., Science 321 (2008) 674–676.
[63] M.S. Chen, D.W. Goodman, Science 306 (2004) 252–255.

[64] H. Xiang, H. Yan, J. Liu, et al., J. Am. Chem. Soc. 144 (2022) 14248–14257.
[65] Z. Zhang, T. Masubuchi, P. Sautet, et al., Angew. Chem. Int. Ed. 62 (2023) e202218210.
[66] T.V.W. Janssens, B.S. Clausen, B. Hvolbæk, et al., Top Catal. 44 (2007) 15–26.
[67] G.N. Vayssilov, Y. Lykhach, A. Migani, et al., Nat. Mater. 10 (2011) 310–315.
[68] C.T. Campbell, Nat. Chem. 4 (2012) 597–598.
[69] H. Zhang, Y. Liu, H. Wu, et al., J. Mater. Chem. A 6 (2018) 20214–20223.
[70] J.X. Wei, M.Z. Cao, K. Xiao, et al., Small Struct. 2 (2021) 2100047.
[71] L. Gong, J. Zhu, F. Xia, et al., ACS Catal. 13 (2023) 4012–4020.
[72] P. Li, G. Zhao, P. Cui, et al., Nano Energy 83 (2021) 105850.
[73] H. Tang, J. Wei, F. Liu, et al., J. Am. Chem. Soc. 138 (2016) 56–59.
[74] M. Smiljanić, S. Panić, M. Bele, et al., ACS Catal. 12 (2022) 13021–13033.
[75] H. Yang, C. Wang, F. Hu, et al., Sci. China Mater. 60 (2017) 1121–1128.
[76] H. Yuan, L. Zhao, B. Chang, et al., Appl. Catal. B 314 (2022) 121455.
[77] J. Zhang, H. B. Yang, D. Zhou, et al., Chem. Rev. 122 (2022) 17028–17072.
[78] Y. Zhu, Q. Lin, Y. Zhong, et al., Energy Environ. Sci. 13 (2020) 3361–3392.
[79] Y. Takabatake, Z. Noda, S.M. Lyth, et al., Int. J. Hydrogen Energy 39 (2014) 5074–5082.
[80] G. Cognard, G. Ozouf, C. Beauger, et al., Appl. Catal. B 201 (2017) 381–390.
[81] B.W. Zhang, L. Ren, Z.F. Xu, et al., Small 17 (2021) 2100732.
[82] X. Li, J. Yu, J. Jia, et al., Nano Energy 62 (2019) 127–135.
[83] X. Cheng, Y. Li, L. Zheng, et al., Energy Environ. Sci. 10 (2017) 2450–2458.
[84] T. Kim, S.B. Roy, S. Moon, et al., ACS Nano 16 (2022) 1625–1638.
[85] Z.W. Wei, H.J. Wang, C. Zhang, et al., Angew. Chem. Int. Ed. 60 (2021) 16622–16627.
[86] X. Fan, C. Liu, B. Gao, et al., Small 19 (2023) 2301178.
[87] Y. Wang, X. Xue, P. Liu, et al., ACS Nano 12 (2018) 12492–12502.
[88] N. Liu, C. Schneider, D. Freitag, et al., Nano Lett. 14 (2014) 3309–3313.
[89] S.R. Chemler, M.T. Bovino, ACS Catal. 3 (2013) 1076–1091.
[90] A.I. Kharlamov, N. V Kirillova, Sov. Powder Metall. Met. Ceram. 22 (1983) 122-134.
[91] D.S. Baek, G.Y. Jung, B. Seo, et al., Adv. Funct. Mater. 29 (2019) 1901217.
[92] D. V. Esposito, S.T. Hunt, Y.C. Kimmel, et al., J. Am. Chem. Soc. 134 (2012) 3025–3033.
[93] C. Cui, R. Cheng, H. Zhang, et al., Adv. Funct. Mater. 30 (2020) 2000693.
[94] Y. Wu, W. Wei, R. Yu, et al., Adv. Funct. Mater. 32 (2022) 2110910.
[95] Z. Li, Z. Qi, S. Wang, et al., Nano Lett. 19 (2019) 5102–5108.
[96] X. Zhao, M. Chen, Y. Zhou, et al., J. Mater. Chem. A 11 (2023) 5830–5840.
[97] G. Chen, H. Wan, W. Ma, et al., Adv. Energy Mater. 10 (2020) 1902535.
[98] H. Yin, Z. Tang, Chem. Soc. Rev. 45 (2016) 4873–4891.
[99] J. Yu, Q. Wang, D. O'Hare, et al., Chem. Soc. Rev. 46 (2017) 5950–5974.
[100] Q. Wang, D. Ohare, 112 (2012) 4124–4155.
[101] Q. Yan, P. Yan, T. Wei, et al., J. Mater. Chem. A 7 (2019) 2831–2837.
[102] R. Subbaraman, D. Tripkovic, D. Strmcnik, et al., Science 334 (2011) 1256–1260.
[103] X. Yu, J. Guo, B. Li, et al., ACS Appl. Mater. Interfaces 13 (2021) 26891–26903.
[104] Y. Feng, Z. Li, S. Li, et al., J. Energy Chem. 66 (2022) 493–501.
[105] W. Zhou, J. Jia, J. Lu, et al., Nano Energy 28 (2016) 29–43.
[106] H. Huang, M. Yan, C. Yang, et al., Adv. Mater. 31 (2019) 1903415.
[107] Z. Ma, H. Tian, G. Meng, et al., Sci. China. Mater. 63 (2020) 2517–2529.
[108] C. Fan, X. Jiang, J. Chen, et al., Small Struct. 2 (2021) 2000017.
[109] X.-K. Wan, H.B Wu, B.Y. Guan, et al., Adv. Mater. 32 (2020) 1901349.
[110] W. Liu, Z. Xiang, A. Tan, et al., Adv. Funct. Mater. 33 (2023) 2212752.
[111] Z. Zhuang, C. Du, P. Li, et al., Electrochim. Acta 368 (2021) 137608.
[112] T. Yang, H. Ling, J.F. Lamonier, NPG Asia Mater. 8 (2016) e240.
[113] J. Liu, N.P. Wickramaratne, S.Z. Qiao, et al., Nat. Mater. 14 (2015) 763–774.
[114] H. Zhang, O. Noonan, X. Huang, et al., ACS Nano 10 (2016) 4579–4586.
[115] J. Zhang, Y. Sun, J. Zhu, et al., Nano Energy 52 (2018) 307–314.
[116] X. Bao, Y. Gong, Y. Chen, et al., J. Mater. Chem. A 7 (2019) 15364–15370.
[117] Q. Cheng, C. Hu, G. Wang, et al., J. Am. Chem. Soc. 142 (2020) 5594–5601.
[118] J. Han, C. Gong, C. He, et al., J. Mater. Chem. A 10 (2022) 16403–16408.
[119] M. Zhang, Q. Dai, H. Zheng, et al., Adv. Mater. 30 (2018) 1705431.
[120] X. Chen, X. An, L. Tang, et al., Chem. Eng. J. 429 (2022) 132259.
[121] H. Zhang, P. An, W. Zhou, et al., Sci. Adv. 4 (2018) eaao6657.
[122] G.R. Bolzan, G. Abarca, W.D.G. Gonçalves, et al., Chem. Eur. J. 24 (2018) 1365–1372.
[123] Q. Hu, G. Li, Z. Han, et al., Adv. Energy Mater. 9 (2019) 1901130.
[124] J. Ren, Y. Zhou, L. Xia, et al., J. Mater. Chem. A 6 (2018) 13835–13847.
[125] J. Li, L. Lin, D. Rui, et al., ACS Nano 11 (2017) 4641–4650.
[126] Y.X. Xiao, J. Ying, J.B. Chen, et al., Chem. Mater. 34 (2022) 3705–3714.
[127] L. Liang, H. Jin, H. Zhou, Nano Energy 88 (2021) 106221.
[128] H. Yang, X. Wang, Adv. Mater. 31 (2019).
[129] Y. Lai, Z. Zhang, Z. Zhang, et al., Chem. Eng. J. 435 (2022) 135102.
[130] L.H. Sun, Q.Y. Li, S.N. Zhang, et al., Angew. Chem. Int. Ed. 60 (2021) 25766–25770.
[131] Y. Liu, Y. Huang, S. Zhou, et al., Inorg. Chem. 62 (2023) 8719–8728.
[132] P. Yin, T. Yao, Y. Wu, et al., Angew. Chem. Int. Ed. 128 (2016) 10958–10963.
[133] Y. Tan, J. Feng, H. Dong,et al., Adv. Funct. Mater. 33 (2023) 2209967.
[134] A. Shan, X. Teng, Y. Zhang, et al., Nano Energy 94 (2022) 106913.
[135] H.D. Mai, S. Jeong, G.N. Bae, et al., J. Alloys Compd. 942 (2023) 169035.
[136] Y. Pei, B. Rezaei, X. Zhang, et al., Mater. Chem. Front. 4 (2020) 2665–2672.
[137] C. Zhang, Y. Cui, Y. Yang, et al., Adv. Funct. Mater. 31 (2021) 2105372.
[138] R.T. Liu, Z.L. Xu, F.M. Li, et al., Chem. Soc. Rev. 52 (2023) 5652–5683.
[139] Q. Feng, X.Z. Yuan, G. Liu, et al., J. Power Sources 366 (2017) 33–55.
[140] Z.Y. Wu, F.Y. Chen, B. Li, et al., Nat. Mater. 22 (2023) 100–108.
[141] W. Li, H. Tian, L. Ma, et al., Mater. Adv. 3 (2022) 5598–5644.
[142] M. Ni, M.K.H. Leung, D.Y.C. Leung, Int. J. Hydrogen Energy 33 (2008) 2337–2354.

43] J. Kibsgaard, I. Chorkendorff, et al., Nat. Energy 4 (2019) 430–433.

44] Y. Luo, Z. Zhang, M. Chhowalla, et al., Adv. Mater. 34 (2022) 2108133.

45] J.W.D. Ng, M. García-Melchor, M. Bajdich, et al., Nat. Energy 1 (2016) 16053.

46] P. Liu, J. Wang, X. Wang, et al., Int. J. Hydrogen Energy 49 (2024) 285–294.

47] T. Zhang, J. Jin, J. Chen, et al., Nat. Commun. 13 (2022) 6875.

48] J. Zhao, J. Wang, X. Zheng, et al., Small Methods 7 (2023) 2201362.

49] J. Gu, L. Li, Y. Xie, et al., Nat. Commun. 14 (2023) 5389.

50] Z. Shi, X. Zhang, X. Lin, et al., Nature 621 (2023) 300–305.

51] S. Dong, C. Zhang, Z. Yue, et al., Nano Lett. 22 (2022) 9434–9440.

52] N. Ai, S. He, N. Li, et al., J. Power Sources 384 (2018) 125–135.

53] S. Kim, D.W. Joh, D.Y. Lee, et al., Chem. Eng. J. 410 (2021) 128318.

54] S. Zhang, W. Wang, F. Hu, et al., Nanomicro Lett. 12 (2020) 140.

55] J. Li, J. Hu, M. Zhang, et al., Nat. Commun. 12 (2021) 3502.

56] M.F. Lagadec, A. Grimaud, et al., Nat. Mater. 19 (2020) 1140–1150.

57] J.T. Ren, L. Wang, L. Chen, et al., Small 19 (2023) 2206196.

58] F.N. Khatib, T. Wilberforce, O. Ijaodola, et al., Renew. Sust. Energ. Rev. 111 (2019) 1–14.

59] M. Chatenet, B.G. Pollet, D.R. Dekel, et al., Chem. Soc. Rev. 51 (2022) 4583–4762.

Declaration of interests

☒ The authors declare that they have no known competing financial interests or personal relationships that could have appeared to influence the work reported in this paper.

☐ The authors declare the following financial interests/personal relationships which may be considered as potential competing interests: